WILEY | Hindawi

Research Article

Obstacle Avoidance Model of Two-Wheeled Vehicles for Nonrigid Obstacles Based on Social Forces

Dan Zhou,[1] **Qingwei Hu** ,[2] **Xin Sun,**[1] **Guobin Gu** ,[3] **Wenyong Li,**[1,2] **and Tao Wang**[1]

[1]*Guangxi Key Laboratory of Intelligent Transportation System (ITS), Guilin University of Electronic Technology, Guilin, China*
[2]*Guangxi Vocational and Technical College of Communications, Nanning 530023, China*
[3]*Guangxi Key Laboratory of International Join for China-ASEAN Comprehensive Transportation, Nanning University, Nanning, Guangxi 530000, China*

Correspondence should be addressed to Qingwei Hu; hqw_199711@163.com

To describe the microtrajectory change behavior of two-wheeled vehicles when encountering nonrigid obstacles, this paper proposes an obstacle avoidance model of two-wheeled vehicles for nonrigid obstacles based on the improved social force method. In the model, the obstacle avoidance characteristics of two-wheeled vehicles for nonrigid obstacles and the safety operation requirements of two-wheeled vehicles are considered. The calculation methods of the minimum boundary distance of avoidance and the boundary avoidance force range edge function are proposed based on the ultimate turning angle and boundary avoidance characteristics, respectively. The speed control and direction control behavior of the rider to the vehicle is abstracted as the form of social force, and the two-wheeled vehicle/rider individual is subjected to the avoidance force and correction force perpendicular to the direction of the longitudinal axis of the vehicle body. The centrifugal trajectory obstacle avoidance motion obeying the Newtonian mechanics is studied based on the characteristics of the vehicle body turning angle change. Different traffic environments are constructed by MATLAB software and simulated according to the model running logic, and sensitivity analysis is performed based on the actual data collected in the survey. The simulation results show that, under the same conditions, compared with $\mu_i = 50$N, when $\mu_i = 200$N, the X-axis displacement of the simulated vehicle in the avoidance process is shortened by 26.31%, and the body deflection angle increases by 50.75% at the end moment of the avoidance process. Compared with electric motorcycles, the displacement of the X-axis in the avoidance process of the electric bicycle is shortened by 16.92%, and the body deflection angle at the end moment of the avoidance process is increased by 13.68%. The simulation results show that the model can well describe the trajectory change behavior characteristics of two-wheeled vehicles/riders encountering nonrigid obstacles in real situations, and the obstacle avoidance model of two-wheeled vehicles proposed in this paper is considered to be traffic justified.

1. Introduction

In recent years, affected by the rapid urbanization, the urban road network has expanded sharply, but in the old urban areas of these cities, there are problems of untimely maintenance of roads and low level of road condition management. Vehicle overloading, poor pavement quality, and tree root extension in the isolation zone lead to road pavement damage problem and poor road evenness. Due to the small traffic load of nonmotorized vehicles, the severity of pavement damage in nonmotorized lanes is generally lower than that in motorized lanes. Because of the light mass of two-wheeled vehicles, the phenomenon of bumping is more obvious when two-wheeled vehicles pass through uneven pavement areas. The vibration filtering capacity of the two-wheeled vehicles' suspension system is limited, which greatly reduces the driving comfort of two-wheeled vehicle riders when passing through the area. Most two-wheeled vehicle riders proactively adjust their riding behavior to change the microtrajectory behavior when passing through the pavement damage area. This paper uses the social force model to modify the characteristics of the microtrajectory change behavior.

The social force model was first used as a pedestrian microdynamics model to study the walking pattern of pedestrians. Pedestrian motion trajectory models in obstacle scenarios [1–6] are a basic class of research based on social force theory. Based on the research foundation, most scholars conduct crowd organization modeling studies in specific scenarios. The study scenarios mainly include airports [7, 8], rail stations [9–11], large shopping malls [12], and other passenger flow distribution locations. In recent years, the study of pedestrian crossing behavior [13–15] has also gradually become a major trend in social force research.

Since there are similarities between pedestrian microdynamics and two-wheeled vehicle microdynamics, some scholars introduced the social force model into the research of two-wheeled vehicle microbehavior. Liang et al. [16] were the first scholars using the social force model to carry out research related to the microdynamics of bicycle flow in nonmotorized lanes. She proposed a classical psychophysiological force model for bicycle riders. The study abstracted bicycles as ellipses and revealed the relationship between vehicles by using driving force, avoidance force, and physiological force. Zheng [17] proposed influencing variables such as riding style and complex interference classification on the basis of the basic psychophysiological force model. She carried out research related to complex traffic phenomena of nonmotorized traffic flow in nonmotorized lanes. Li [18] proposed a microscopic behavior model of bicycles at signalized plane intersections based on the social force model. Some other scholars have used social force models to modify the characteristics of traffic conflicts in shared spaces between motor vehicles and nonmotor vehicles and humans and nonmotor vehicles. The research related to the motor vehicle-nonmotor vehicle microdynamics focuses on the interference phenomenon generated by nonmotorized vehicles intruding into the motor vehicle passing area. These research studies established the related social force dynamics model based on the interference characteristics. The study scenarios of the motor vehicle-nonmotor vehicle microdynamics model mainly include motor vehicle-nonmotor vehicle shared traffic areas such as single carriageway road, dual carriageway road [19, 20], and intersection areas [21, 22]. The relevant human-nonmotor vehicle microdynamics model not only studies the disturbing effect of pedestrians on two-wheeled vehicles [23, 24] but also considers the disturbing behavior of two-wheeled vehicles on pedestrians [25]. Moreover, scholars have carried out studies related to the interaction between crosswalks and two-wheeled vehicles [26], which further improved the research system of microdynamics of slow-traffic mixed traffic flow. A comparison of the various social force modeling approaches is shown in Table 1.

In summary, at present, research on the driving behavior of motor vehicle drivers and autonomous vehicles is relatively mature [33], but there is relatively little research on the driving behavior of two-wheeled vehicles' rider in special environments; the existing two-wheeler microdynamics studies based on the social force model are mainly modeled for obstacles such as two-wheelers, four-wheeled motor vehicles, road boundaries, and pedestrians, which may not

be traversed from the top of such obstacles during the normal operation of a two-wheeler. These obstacles are rigid obstacles. Therefore, when two-wheeled vehicles are interfered by such obstacles, pedestrians choose to avoid or follow the obstacles, and the existing literature mainly focuses on the modeling study of the operation characteristics of the above rigid obstacles. In this paper, the focus of obstacles is shifted to the type of nonrigid obstacles such as road breaks and speed bumps. Taking the microscopic trajectory of obstacle avoidance behavior of two-wheeled vehicles as the object of study, based on the method of the social force model, considering the change of body angle, and innovatively introducing the concepts of avoidance force and modification force, we propose a two-wheeled vehicle nonrigid obstacle avoidance model with a view to providing two-wheeled vehicle drivers with suggestions for safe driving.

2. Model Preparation

2.1. Definition of Nonrigid E Obstacles.
This paper defines objects that interfere with the movement of two-wheeled vehicles within the nonmotorized lanes (including the lane boundaries) as obstacles, where the concept of nonrigid obstacles is defined according to the characteristics of the obstacles. Static disturbing objects in nonmotorized lanes are defined as nonrigid obstacles that can be rolled over in the normal operation of two-wheeled vehicles, produce discomfort (including vehicle vibration and water splashing) when contacted at low and medium speeds, and produce operational safety problems caused by violent vehicle bumps when contacted at high speeds. Among these nonrigid obstacles, there are pavement damage subsidence within 10 cm, shallow puddles, and speed bumps. When disturbed by a flexible obstacle, the rider passes in a more selective way, either by avoiding the obstacle or by rolling over the obstacle with safety in mind.

2.2. Vehicle Body Deflection Angle.
When a two-wheeled vehicle is in the process of the avoidance, the angle at which the body axis is deflected within a certain period of time is called the vehicle body deflection angle. Assuming that the body axis is parallel to the driving direction of the lane at moment 0 s and the avoidance behavior is about to start, the vehicle body deflection angle at moment t_0 is defined as $\theta(t_0)$, and the change of the vehicle body deflection angle generated in the next unit time interval Δt is $\Delta \theta(t_0)$. The diagram of the vehicle body deflection angle is shown in Figure 1, in which the vehicle body deflection angle reference line is the line in the direction of the central axis of the vehicle body at the last unit moment.

2.3. Extreme Avoidance.
As shown in Figure 2, point Q is the starting point for the vehicle to start avoiding (the point where the front wheel of the vehicle makes contact with the ground). Point R is the crossing point of the vehicle avoidance trajectory (the trajectory of the contact point between the front wheel and the ground) and the central axis

TABLE 1: Summary of modeling methods in the society.

| No.	Year	Methodological features	Authors
1	2022	A microscopic simulation model of the overtaken vehicle is constructed by studying the behavior of the overtaken vehicle's lateral offset and longitudinal deceleration and avoidance during proximity overtaking, based on the social force model, introducing the kinetic energy weight coefficients to improve the repulsion force, and improving the driving force by taking into account the effect of the headway spacing on the desired speed	Zhang et al. [27]
2	2022	Based on the pedestrian avoidance mechanism, the social force model in any logic pedestrian library is improved, and the simulation parameters are optimally adjusted by taking into account the impact of short-time passenger impact on station operation organization	Wang et al. [28]
3	2021	To address the phenomenon of unreasonable contact between opposing pedestrians, the contact theory of the particle discrete element model is introduced into the social force model to restore the contact behavior between pedestrians in the opposing channel	Shang et al. [29]
4	2019	It gives a new approach to take advantage of "appropriate" psychological forces induced by gravity to enhance evacuation efficiency	Kang et al. [30]
5	2014	The stochastic adjustment mechanism by speed changing and direction changing was developed, which enables to effectively solve the problems in simulation that two conflicting pedestrians may collide or stop forever due to social force balance	Zeng et al. [31]
6	2009	The modification consists of a respect area parameterized by the respect factor, RF, that provides a simple self-stopping mechanism to prevent a pedestrian from continuously pushing into other pedestrians in his/her way	Parisi et al. [32]
7	2023	Taking the obstacle avoidance trajectory of a two-wheeled vehicle travelling in the upstream virtual passing zone as the research object, both the acceleration and deceleration behaviors of the two-wheeled vehicle and the control of the vehicle's faucet are abstracted into the form of social forces, and the conventional nonmotorized vehicle social force model is improved to establish a nonrigid obstacle avoidance model	Author of this article
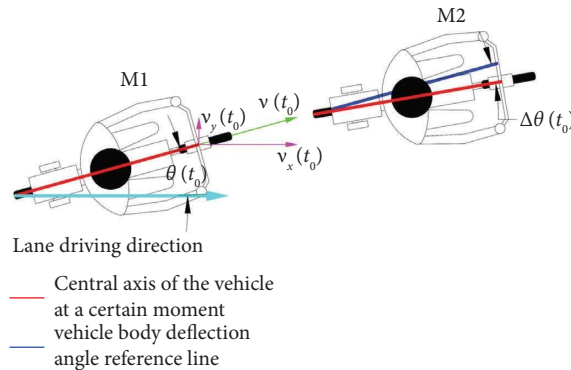
FIGURE 1: Diagram of the deflection angle of the vehicle body.

of the damaged area. Point P is the projection point of point Q on the central axis of the damaged area. Points C and D are the crossing points of the edge line of the damaged area on the left and right side of the driving direction and the central axis of the damaged area, respectively. Along points C and D, 2 lines extend parallel along the upstream direction of the lane, defined as the upstream virtual traffic zone boundary. The area between the 2 lines is the upstream virtual traffic zone. The length of RC is l, m. The length of CP is L_1, m. The length of PD is L_2, m. The length of QP (avoidance distance) is S, m.

Due to the influence of external interference or other factors, the rider does not recognize the flexible obstacle within the safety recognition distance, and when the avoidance distance reaches the minimum value, there is an extreme avoidance problem. In the process of extreme

avoidance, the trajectory from Q to R can be simplified to a straight line, which is the QR line in Figure 2. The vehicle body deflection angle change process can be approximately considered as the body deflection angle does not continue to change after reaching the extreme body deflection angle at the fastest angular speed until the vehicle front wheel passes the point R. ∠PQR can be approximately used as the extreme vehicle body deflection angle θ_{max}.

The extreme vehicle body deflection angle θ_{max} will be variable under different speed conditions. From the literature [34], it is known that, under the same conditions, the larger the speed, the smaller the extreme body deflection angle θ_{max}. The extreme vehicle body deflection angle satisfies the requirement of equation (1). Based on the extreme vehicle body deflection angle θ_{max}, the extreme avoidance distance S_{min} of the vehicle can be calculated by the vehicle speed and vehicle lateral position. The extreme avoidance distance satisfies the requirement of equation (2).

$$\theta_{max} = \frac{d}{(0.48v + 0.86)}, \tag{1}$$

$$S_{min} = \frac{\left[\min\left(L_1, L_2\right) + (\delta/2)\right]}{\tan \theta_{max}}, \tag{2}$$

where d is the wheel diameter of the vehicle, m; δ is the wheel width of the vehicle, m; v is the speed, m/s. After a survey of the mainstream two-wheeled brands in the market, it was concluded that the majority of two-wheeled vehicles have a wheel diameter of 14 in and a tire width of 5.40 cm. The majority of electric motorcycle wheels are 10 in in wheel diameter and 7.62 cm in tire width. Most of the wheels of human-powered bicycles have a wheel diameter of 24 in–26 in and a tire width of 3.49–4.95 cm. Under the condition that the initial vehicle body deflection angle is 0 rad, the value of S_{min} varies with wheel diameter, speed, and vehicle lateral position. The value variations of S_{min} are shown in Figure 3.

Based on the vehicle operation state under the extreme avoidance condition, the speed and trajectory constraints of the vehicle are proposed. The trajectory constraints are shown in equation (3), and the speed constraints are shown in equation (4).

$$\text{s.t.} = \begin{cases} X: x(0) = S \geq S_{min}, \\ Y: 0 \leq y(t) \leq \min\left(S. \cos \theta_{max}, C_\beta + L_\alpha\right), \\ L_\alpha = \min(L_\alpha), \alpha \in (1, 2), \\ \beta \in l, \alpha = 1, \\ \beta \in r, \alpha = 2, \end{cases} \tag{3}$$

$$\text{s.t.} \begin{cases} X: \left\|\overrightarrow{v}_x(t)\right\| \leq \left\{\left[\dfrac{d}{|0.12\Delta\theta(t)|}\right] - 1.79\right\} \cdot \cos \theta(t), \\ Y: \left\|\overrightarrow{v}_y(t)\right\| \leq \left\{\left[\dfrac{d}{|0.12\Delta\theta(t)|}\right] - 1.79\right\} \cdot \sin \theta(t), \end{cases}$$
$$\tag{4}$$

where C_β is the vertical distance between the crossing point (points C or D) and the edge line of the lane, m. If $\beta \in l$, C_β represents the distance to the left of the lane driving direction. If $\beta \in r$, C_β represents the distance to the right of the lane driving direction.

2.4. Individual Vehicle Scope and Area Coordinates.
Vehicle individual scope definition includes 2 categories: vehicle body scope and driving field scope. Vehicle body scope is the physical scope of the vehicle body. The driving filed scope is a more comfortable clearance area around the vehicle when the rider rides [35]. The scopes of individuals in 2 categories are shown in Figure 4.

The center of the ellipse is the midpoint of the line connecting the contact points between the front and rear wheels of the vehicle and the ground. The major and minor semiaxes of the ellipse of the vehicle body scope are a_i and b_i, respectively. The major and minor semiaxes of the ellipse of the driving field scope are a_s and b_s, respectively. The range of ellipse calculation function is shown in equation (5) [36].

$$\left(\frac{x^2}{a_\eta^{\,2}}\right) + \left(\frac{y^2}{b_\eta^{\,2}}\right) = 1, \eta \in (i, s). \tag{5}$$

Calculation functions for the major and minor semiaxes of the scope of the human-powered bicycle and the scope of the driving field:

$$\begin{cases} a_i = 1, \\ b_i = 0.45, \\ a_s = 0.85e^{0.0887v}, b_s = 0.3e^{0.1043v}, \quad v > 3.89\dfrac{m}{s}, \\ a_s = 1, b_s = 0.45, \qquad\qquad\quad v \leq 3.89\dfrac{m}{s}. \end{cases} \tag{6}$$

Calculation functions for the major and minor semiaxes of the scope of the electric two-wheeled vehicle and the scope of the driving field:

$$\begin{cases} a_i = 1, \\ b_i = 0.55, \\ a_s = 0.75e^{0.1209v}, b_s = 0.39e^{0.0877v}, \quad v > 3.89\dfrac{m}{s}, \\ a_s = 1, b_s = 0.55, \qquad\qquad\quad v \leq 3.89\dfrac{m}{s}. \end{cases} \tag{7, 8}$$

In this section, for the convenience of later modeling, the scope of the flexible obstacle and the surrounding area is divided by the definition of coordinates. This paper takes midpoint O of line CD as the origin, the upstream direction of driving direction is the positive direction of X-axis, and the left direction of driving direction is the positive direction of Y-axis, as shown in Figure 5.
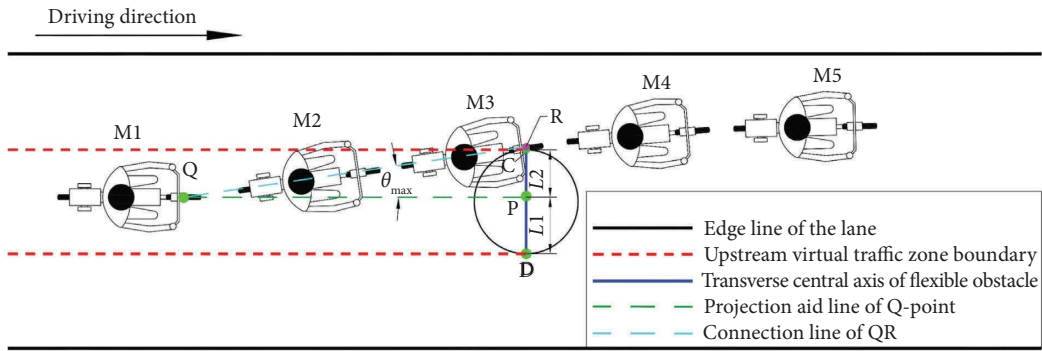
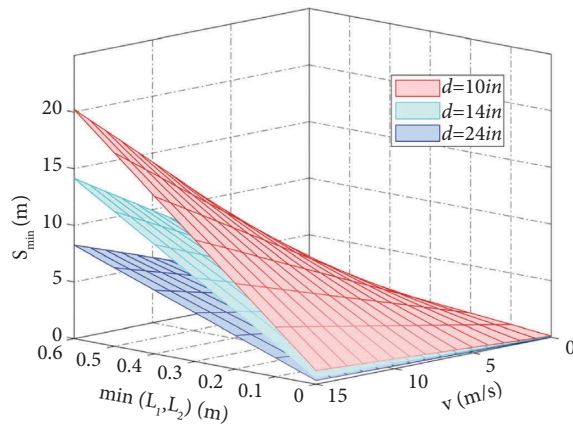FIGURE 2: Diagram of extreme state avoidance trajectory.

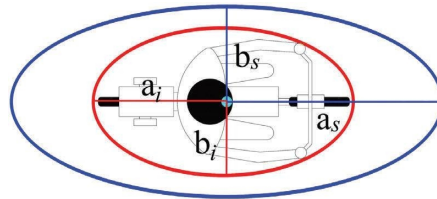FIGURE 3: Value variation of extreme avoidance distance.
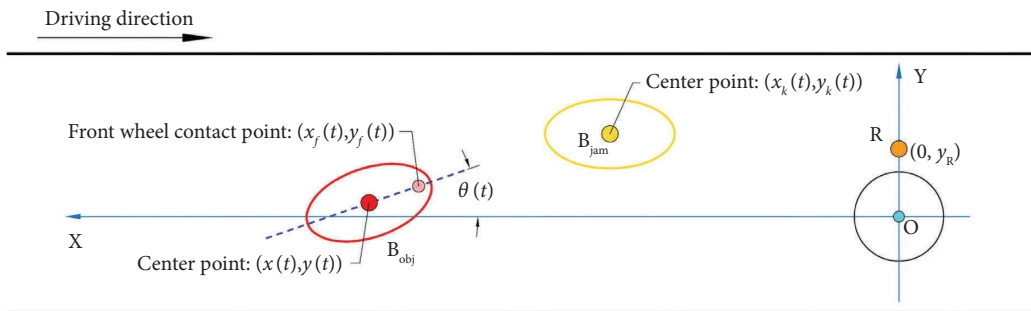

FIGURE 4: Vehicle individual scope.

FIGURE 5: Area coordinate division.

In Figure 5, B_{obj} is the subject vehicle of the study. B_{jam} is the surrounding interference vehicle. The center position coordinate of the vehicle B_{obj} at moment t is $(x(t), y(t))$. The coordinate of point R is $(0, y_R)$.

$$|y_R| = \left(\frac{w}{2}\right) + l, \tag{9}$$

where w is the width value of the axis of the flexible obstacle in the direction perpendicular to the driving direction, m (shown in Figures 4–6). The horizontal and longitudinal coordinates of the contact point σ between the front wheel of the subject vehicle B_{obj} and the ground at moment t are given in the following equation.

$$\begin{cases} x_f(t) = x(t) - \left[a_i - \left(\frac{d}{2}\right)\right] \cdot \cos \theta(t), \\ \\ y_f(t) = y(t) + \left[a_i - \left(\frac{d}{2}\right)\right] \cdot \sin \theta(t), \end{cases} \tag{10}$$

where $x_f(t)$ is the horizontal coordinate of the contact point σ between the front wheel of the subject vehicle B_{obj} and the ground at moment t. $y_f(t)$ is the longitudinal coordinate of the contact point σ between the front wheel of the subject vehicle B_{obj} and the ground at moment t. $\theta(t)$ is the vehicle body deflection angle of the subject vehicle B_{obj} at moment t.

3. Modeling

3.1. The Action Scope of Social Forces

3.1.1. Minimum Boundary Distance of Avoidance. The concept of minimum boundary of avoidance is proposed for the constraint of the extreme body deflection angle in actual avoidance. When the contact point $(x_f(t), y_f(t))$ between the front wheel of the vehicle and the ground belongs to the area between the minimum boundary and the edge of the flexible obstacle, the vehicle will no longer change the effect of the lateral avoidance force on the obstacle (as shown in Figure 7). Under this speed and position condition, the vehicle is no longer able to completely avoid the flexible obstacle. The rider abandons the need for avoidance and focuses more on the constraints for the desired speed to get better safety and comfort.

The minimum boundary of avoidance is related to the speed, vehicle body deflection angle, and lateral position of the vehicle. As the vehicle speed changes, the minimum boundary changes accordingly. The minimum boundary function $x_a(t)$ is shown in equation (11).

Taking subsidence of manhole cover as the research object, the diameter of the subsidence area is assumed as 0.8 m, $\theta(t) = 0$, and the minimum boundary ranges for different wheel types (refer to Section 2.3) and speeds are shown in Figure 6. The schematic of minimum boundary is shown in Figure 8.

$$x_a(t) = \frac{\left[(w/2) - |y_f(t)| + (\delta/2)\right]}{\tan\left\{[d/(0.48v(t) + 0.86)] + \theta(0) + \int \Delta\theta(t)dt\right\}}, y_f(t) \in \left(-\frac{w}{2}, \frac{w}{2}\right). \tag{11}$$

3.1.2. Boundary Avoidance Force Range. The vehicle body deflection angle and speed at a certain moment produce a boundary avoidance range, which will change in real time with the change of the vehicle body deflection angle and speed. When the front wheel of the vehicle rides into the boundary avoidance area, the vehicle is then subjected by the boundary avoidance force. Assume that the vehicle is riding with the current vehicle body deflection angle and speed at the moment t_1, the angular speed and vehicle speed will change after being subjected to the correction avoidance force. The body deflection angle is changed with the uniform angular speed of $\Delta\theta(t_1)$. The vehicle speed is corrected with $v(t)$. The correction ends when the vehicle corrected lateral

speed reaches 0 m/s and has conflict with the lane virtual boundary. At the moment t_1, the absolute value of the longitudinal coordinate of the vehicle front wheel contact point is the value of the width of the boundary avoidance force range H_{min}, m. The lane virtual boundary is the minimum safe distance boundary acceptable to the rider from the lane boundary, and its distance from the lane boundary is the difference between the driving filed scope and the minor semiaxis of the vehicle scope. The boundary avoidance force range diagram is shown in Figure 7, calculation function H_{min} is shown in equation (12), and the boundary avoidance force range edge function is shown in equation (13).

$$\begin{cases} H_{min}(t) = \int_{t_1}^{t_2} \left\{v(t) \cdot \sin\left[|\theta(t)| - |\Delta\theta(t_1)| \cdot (t - t_1)\right]\right\}dt + b_s, \\ \\ t_2 = \left|\frac{\theta(t_1)}{\Delta\theta(t_1)}\right| + t_1, \end{cases} \tag{12}$$
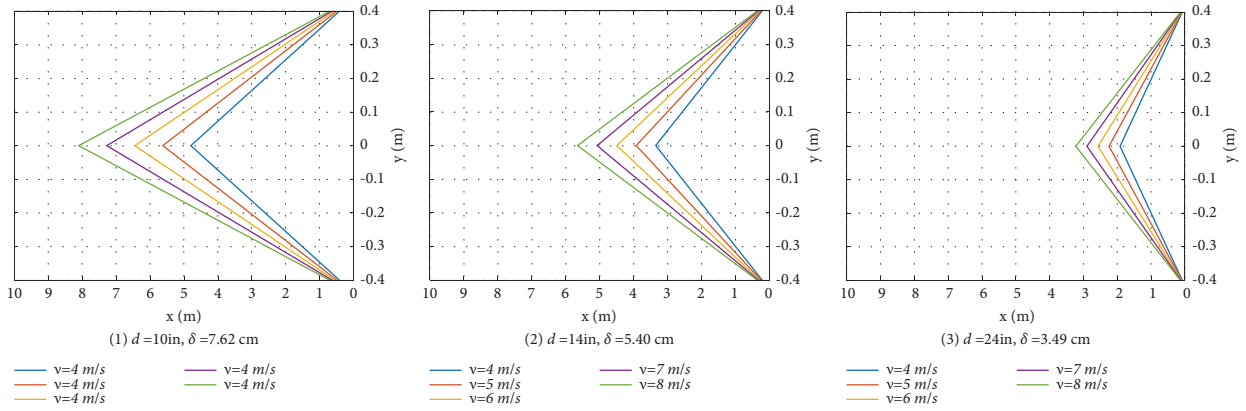
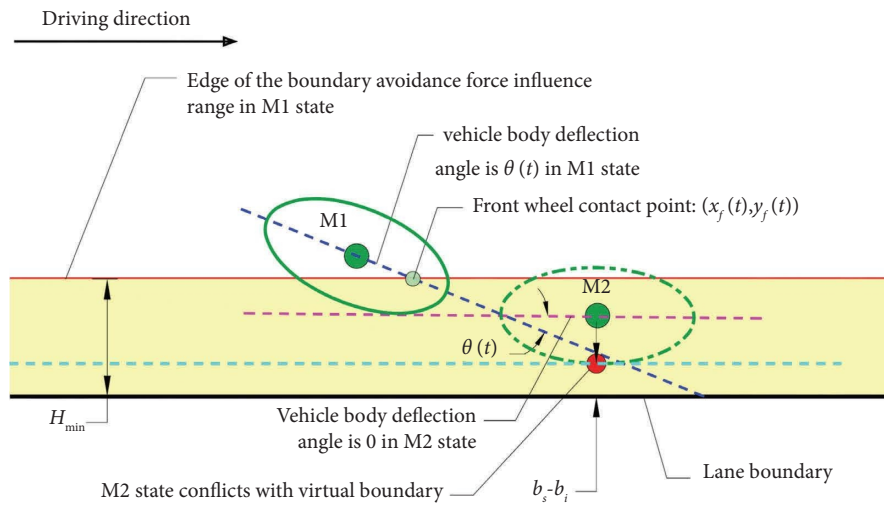Figure 6: Minimum boundary range of avoidance.

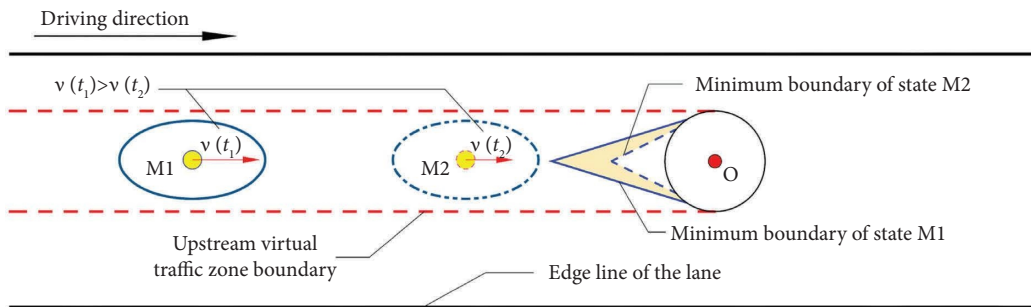Figure 7: Boundary avoidance force range.

Figure 8: Diagram of the minimum boundary of avoidance.

$$y_b(t) = \begin{cases} C_l + \left(\dfrac{w}{2}\right) - H_{\min}(t), x_f(t) \in \left(\dfrac{w}{2}, C_l + \left(\dfrac{w}{2}\right)\right), \\[3mm] H_{\min}(t) - C_r - \left(\dfrac{w}{2}\right), -x_f(t) \in \left(\dfrac{w}{2}, C_l + \left(\dfrac{w}{2}\right)\right), \end{cases} \tag{13}$$

where t_1 is the moment when the vehicle discriminates the boundary avoidance force range, s. t_2 is the moment when the body deflection angle is changed to 0 rad by the modified driving force, s. As shown in Figure 5, C_l is the distance between point C and the left boundary of the lane driving direction, m. C_r is the distance between point C and the right boundary of the lane driving direction, m.

3.2. Driving Force Model.

Obstacle driving force is a psychological force that only changes the vehicle speed. It is an expression of the rider's desire to obtain a comfortable riding experience by acceleration or deceleration when encountering a flexible obstacle. The driving force $\overrightarrow{F}_{l,d}(t)$ is related to the desired speed $v_{\exp}$ of the rider. However, when the horizontal coordinate $x_f(t)$ of the front wheel contact point is less than the minimum avoidance boundary $x_a(t)$ to $y_f(t)$, the rider cannot perform effective avoidance behavior under the speed, body deflection angle, and position conditions. The rider performs deceleration considering more the comfort when rolling through the flexible obstacle, as well as considering the comfortable desired speed $v_{\exp}^{\mathrm{com}}$. In this paper, the moment when the vehicle starts the avoidance behavior is set to $t = 0$. The vehicle driving force calculation function of the upstream of the flexible obstacle is shown in the following equation.

$$\overrightarrow{F}_{l,d}(t) = \begin{cases} m_i \cdot \left\{ \dfrac{\left[v_{\exp}^{\mathrm{avo}}(t) - v(t)\right]}{\Delta t_{\exp}^{\mathrm{avo}}} \right\} \overrightarrow{n}_a, & x_f(t) \ge x_a(t), t \in [0, t_{\mathrm{avo}}), \\[5mm] m_i \cdot \left\{ \dfrac{\left[v_{\exp}^{\mathrm{com}}(t) - v(t)\right]}{\Delta t_{\exp}^{\mathrm{com}}} \right\} \overrightarrow{n}_a, & x_f(t) < x_a(t), t \in [0, t_{\mathrm{avo}}), \end{cases} \tag{14}$$

where m_i is the mass of the subject vehicle i. $v(t)$ is the actual riding vehicle speed at the moment t. $v_{\exp}^{\mathrm{avo}}(t)$ is the vehicle comfortable desired speed at moment t. $\Delta t_{\exp}^{\mathrm{avo}}$ is the expected action duration of the rider to achieve the desired speed of avoidance. $\Delta t_{\exp}^{\mathrm{com}}$ is the expected action duration of the rider to achieve the comfortable desired speed. t_{avo} is the moment when the front wheel of the vehicle reaches the point R. $\overrightarrow{n}_a$ is the unit vector along the major semiaxis of the body scope towards the front of the vehicle.

3.3. Avoidance Forces and Correction Forces Model

3.3.1. Obstacle Avoidance Force.

Obstacle avoidance force $\overrightarrow{F}_{t,a}(t)$ is a mental force generated by the rider to avoid a flexible obstacle (as in the M1–M3 states in Figure 9). The force explains the behavior of a rider steering a two-wheeled vehicle to change its body deflection angle after encountering a flexible obstacle. This behavior does not change the speed in the direction of the major semiaxis of the body scope and only changes the direction of the major semiaxis of the body scope. The obstacle avoidance force is always perpendicular to the direction of the major semiaxis of the vehicle body scope, which does not change the vehicle speed and only changes the vehicle body deflection angle.

The value of the obstacle avoidance force depends on the distance between the vehicle and the minimum avoidance boundary. Obstacle avoidance force disappears after the vehicle leaves the upstream virtual traffic zone. As shown in Figure 9, the force expressed by dotted line in the M3 state indicates the disappearance of $\overrightarrow{F}_{t,a}(t)$. The calculation function of obstacle avoidance force is shown in the following equation.

$$\overrightarrow{F}_{t,a}(t) = \begin{cases} \mu_i \cdot \exp\left\{ -\dfrac{\left[x_f(t) - x_a(t)\right]}{x_f(t)} \right\} \cdot \overrightarrow{n}_v, & x_f(t) \ge x_a(t), t \in \left[0, t_{\mathrm{avo}}^1\right), \\[5mm] \mu_i \cdot \overrightarrow{n}_v, & x_f(t) < x_a(t), t \in [0, t_{\mathrm{avo}}), \\[5mm] 0, & t \in [t_{\mathrm{avo}}, +\infty), \end{cases} \tag{15}$$
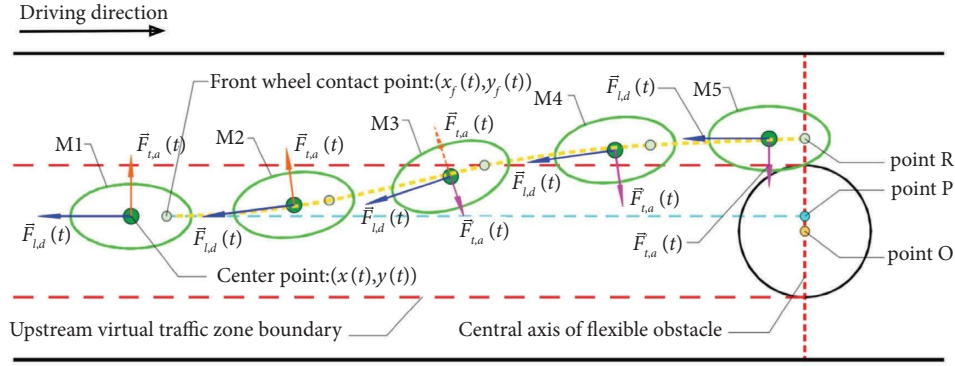
FIGURE 9: Force diagram of obstacle avoidance force and avoidance correction force.

where μ_i is the strength of obstacle avoidance force for individual i and the value of μ_i is certain for the specific subject vehicle. t_{avo}^1 is the moment when the vehicle leaves the upstream virtual traffic zone and the front wheel rolls over the boundary of the upstream virtual traffic zone. t_{avo} is the moment when the vehicle passes the point R. $\overrightarrow{n}_v$ is the unit vector perpendicular to the direction of the major semiaxis of the body scope.

3.3.2. Front Vehicle Correction Avoidance Force.
When a rider discovers an interfering vehicle in the influence area ahead, the interfering vehicle exerts a psychological pressure on the rider, which forms the front vehicle correction avoidance force $\overrightarrow{F}_{v,a}^f(t)$. The force affects the rider's choice of the avoidance behavior. When the front vehicle correction avoidance force is too large, it causes the rider to abandon the avoidance behavior and to roll over the flexible obstacle by reducing the expected speed. The vehicle trajectory under the action of the front vehicle correction avoidance force is shown in Figure 10.

If the speed of the frontal interfering vehicle is less than the speed of the subject vehicle, the psychological pressure of the interfering vehicle on the rider keeps increasing as the longitudinal distance between the two vehicles continuously decreases. When the speed of the front interference vehicle is smaller than the speed of the subject vehicle, the rider does not choose the avoidance behavior and the front vehicle correction avoidance force is equal to the obstacle avoidance force. When the front vehicle is overtaken by the subject vehicle in the longitudinal direction, the front vehicle correction avoidance force disappears. When the speed of the front interference vehicle is too fast (this paper defines the speed of the front interfering vehicle as greater than or equal to 1.5 times the speed of the subject vehicle), the rider thinks that the front interference vehicle does not cause interference to himself and the front vehicle correction avoidance force is 0 N.

The value $r_p(t)$ of the longitudinal length of the frontal influence area varies with speed. The value varies for riders of different personalities and relies heavily on the subjective thoughts of the riders. This paper assigns a fixed value to the longitudinal length of the frontal influence area according to the personalities of different riders and vehicle speed. When the longitudinal distance between the interfering vehicle and the subject vehicle is within the value of the longitudinal length of the frontal influence area, the rider is subjected to the front vehicle correction avoidance force. The calculation formula of the value $r_p(t)$ of the longitudinal length of the frontal influence area is shown in equation (16). The calculation formula of the value r_h of the horizontal width of the frontal influence area is shown in equations (17) and (18). The frontal influence area is shown in Figure 11.

The value of front vehicle correction avoidance force depends on the difference in speed and distance between the two vehicles along the X-axis. In general, under the same conditions, the smaller the difference in speed and distance, the larger the front vehicle correction avoidance force. If the front wheel of the subject vehicle rolls over the upstream virtual traffic zone boundary, the front vehicle correction avoidance force disappears. The mental force expressed by the dotted line B_{obj} of M3 state in Figure 11 indicates the front vehicle correction avoidance force disappears. The calculation function of the front vehicle correction avoidance force is shown in equation (19).

$$r_p(t) = \kappa_i\left(\left[\frac{v(t) \cdot t_{rea}}{3.6}\right] + \left[\frac{v^2(t)}{(254\phi)}\right] + I_{saf}\right), \tag{16}$$

$$r_h = \left|(-1)^\lambda\left(\frac{w}{2}\right) - y(0)\right| + b_{s,i}(t) + b_{i,k}(t), \tag{17}$$

$$\lambda = \begin{cases} 0, & B_{obj} \text{ detour to right,} \\ 1, & B_{obj} \text{ detour to left,} \end{cases} \tag{18}$$
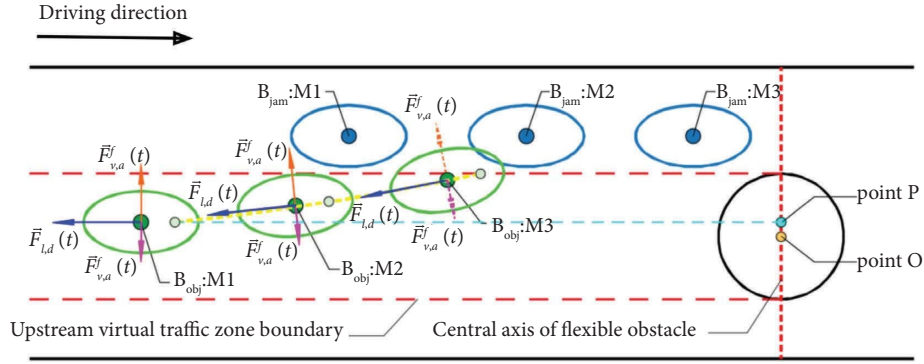
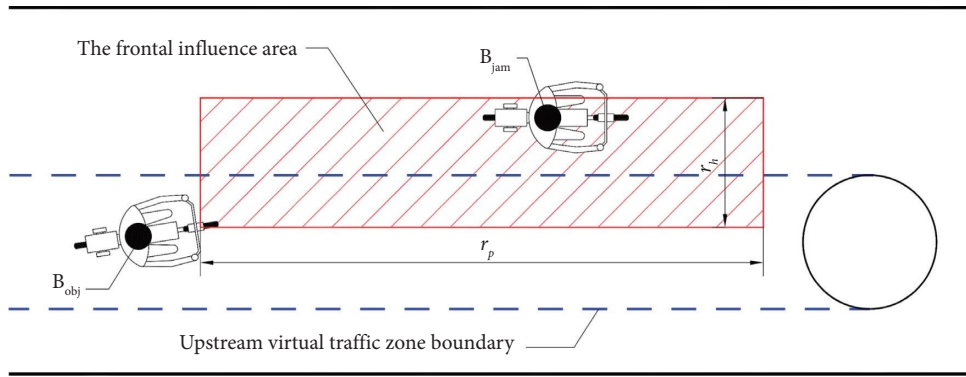FIGURE 10: The vehicle trajectory under the action of the front vehicle correction avoidance force.

FIGURE 11: Diagram of the frontal influence area.

$$
\overrightarrow{F}_{v,a}^{f}(t) = \begin{cases} \left\| \overrightarrow{F}_{t,a}(t) \right\| \cdot \exp\left\{ \dfrac{-\left[x(t) - a_{s,i}(t) - x_{k,b}(t)\right]}{r_p(t)} \right\} \cdot \left[\dfrac{v_x(t)}{v_k(t)}\right] \cdot \overrightarrow{n}_v', & \begin{aligned} & x_{k,b}(t) \in \left[x(t) - r_p(t), x(t) - a_{s,i}(t)\right] \\ & y_k(t) \in \left[\dfrac{w}{2}, r_h + \left(\dfrac{w}{2}\right)\right] \\ & \left|y_f(t)\right| \in \left[0, \dfrac{w}{2}\right) \\ & v_k(t) \in \left[v_x(t), 1.5v_x(t)\right] \end{aligned} \\[2em] 0, & \begin{aligned} & x_{k,b}(t) \in \left[x(t) - r_p(t), -\infty\right] \\ & y_k(t) \notin \left[\dfrac{w}{2}, r_h + \left(\dfrac{w}{2}\right)\right] \\ & \left|y_f(t)\right| \notin \left[0, \dfrac{w}{2}\right) \\ & v_k(t) \in \left[1.5v_x(t), +\infty\right] \end{aligned} \end{cases} \tag{19}
$$

where κ_i is the personality correction parameter for the longitudinal length of the influence area ahead of the subject individual i. The number is a certain value for the specific subject vehicle. $x_{k,b}(t)$ is the horizontal coordinate of the projection of the rear of the interfering vehicle on the

ground. t_{rea} is the rider's reaction time, s. ϕ is the friction coefficient of the tire. I_{saf} is the safety distance, m. $a_{s,i}(t)$ is the length of the major semiaxis of the driving field scope of the subject individual i at moment t. $b_{s,i}(t)$ is the length of the minor semiaxis of the driving field scope of the subject

individual i at moment t. $b_{s,k}(t)$ is the length of the minor semiaxis of the vehicle body scope of the subject individual k at moment t.

When $y_k(t) \in [w/2, r_h + (w/2)]$, $v_k(t) \in [0, v_x(t))$ or $x_{k,b}(t) \in [x(t) - a_{s,i}(t), x(t)]$, the rider of the subject vehicle is under great psychological pressure from the interfering vehicles, the rider is not willing to avoid. The calculation formula of front vehicle correction avoidance force is shown in the following equation.

$$\overrightarrow{F}^f_{v,a}(t) = \left\| \overrightarrow{F}_{t,a}(t) \right\| . \overrightarrow{n}'_v. \tag{20}$$

When the subject vehicle is subjected to the front vehicle correction avoidance force, the change of the vehicle body deflection angle is controlled by the combined force of the collision avoidance force and the front vehicle correction avoidance force. This paper defines that the combined force of all social forces other than the driving force is called the combined force of avoidance. The combined force only controls the driving direction of the vehicle and not the vehicle speed. The calculation function of change rate of the body deflection angle is shown in the following equation.

$$\Delta\theta(t) = \frac{\left\| \overrightarrow{F}_{t,a}(t) + \overrightarrow{F}^f_{v,a} \right\|}{[m_i.v(t)]}, \left| y_f(t) \right| \in \left[0, \frac{w}{2} \right). \tag{21}$$

If the rider expects to avoid the flexible obstacle, the vehicle trajectory during the avoidance duration Δt^1_{avo} needs to satisfy the condition shown in the following equation.

$$\text{s.t.} \begin{cases} y(0) + \int_0^{t^1_{avo}} v(t). \sin\left[\theta(0) + \int \Delta\theta(t) dt \right] dt + \left[a_i - \left(\frac{d}{2} \right) \right] \sin\theta\left(t^1_{avo} \right) = \frac{0.5w.y_f(0)}{\left| y_f(0) \right|}, \\[4mm] x(0) - \int_0^{t_{avo}} v(t). \cos\left[\theta(0) + \int \Delta\theta(t) dt \right] dt - \left[a_i - \left(\frac{d}{2} \right) \right] \cos\theta\left(t^1_{avo} \right) \ge 0. \end{cases} \tag{22}$$

3.3.3. Obstacle Avoidance Correction Force.

Obstacle avoidance correction force $\overrightarrow{F}'_{t,a}(t)$ is a psychological force generated by the rider to correct the vehicle operation after riding away from the upstream virtual traffic zone (shown in M3–M5 states in Figure 9). After the front wheel of the vehicle rides away from the upstream virtual traffic zone boundary, the rider steers the vehicle and corrects the direction as soon as possible to make the vehicle driving direction parallel to the lane driving direction. The rider deflects the vehicle toward the center of the lane so that the body deflection angle is corrected to 0 rad as soon as possible, to avoid collision between the vehicle and the lane boundary. The obstacle avoidance correction force is always perpendicular to the major semiaxis speed direction of the vehicle body scope. The value of the obstacle avoidance correction force depends on the distance between the vehicle and the edge of the boundary avoidance force influence range. After the vehicle leaves the upstream virtual traffic zone, the obstacle avoidance correction force disappears when the vehicle body deflection angle is corrected to 0 rad. The constraint function of the end moment of the obstacle avoidance correction force is shown in equation (23). The calculation function of the obstacle avoidance correction force is shown in equation (24). The calculation function of the change rate of the body deflection angle under the action of the obstacle avoidance correction force is shown in equation (25).

$$\begin{aligned} \theta\left(t^3_{avo} \right) &= \theta(0) + \int_0^{t^3_{avo}} \Delta\theta(t) dt \\ &= 0, t^3_{avo} > t^1_{avo}, \end{aligned} \tag{23}$$

$$\overrightarrow{F}'_{t,a}(t) = \begin{cases} \rho_i. \exp\left\{ -\left| \frac{[y_f(t) - y_b(t)]}{[|y_b(t)| - (w/2)]} \right| \right\}. \overrightarrow{n}'_v, & \left| y_f(t) \right| \in \left[\frac{w}{2}, y_b(t) \right) \& t \in \left[t^1_{avo}, t^3_{avo} \right), \\[4mm] 0, & \left| y_f(t) \right| \in \left[0, \frac{w}{2} \right) \wedge t \in \left[t^3_{avo}, +\infty \right), \end{cases} \tag{24}$$

$$\Delta\theta(t) = \frac{\left\| \overrightarrow{F}'_{t,a}(t) \right\|}{[m_i.v(t)]}, \left| y_f(t) \right| \in \left[\frac{w}{2}, y_b(t) \right) \& t \in \left[t^1_{avo}, t^3_{avo} \right), \tag{25}$$

where ρ_i is the strength of the obstacle avoidance correction force for individual i. The value of ρ_i is a certain value for the specific subject vehicle. $\overrightarrow{n}_v'$ is the unit vector in the direction opposite to $\overrightarrow{n}_v$ and perpendicular to the direction of the major semiaxis of the body scope. For example, if $\overrightarrow{n}_v'$ is oriented to the left of the lane driving direction, then $\overrightarrow{n}_v$ is oriented to the right of the lane driving direction. The function of the vehicle front wheel trajectory in the flexible obstacle section without the boundary avoidance force condition is shown in the following equation.

$$
\begin{cases}
x_f(t) = x(0) - \left[a_i - \left(\dfrac{d}{2}\right)\right]\cos\theta(t) - \displaystyle\int_0^t v(t).\cos\left[\theta(0) + \int \Delta\theta(t)\mathrm{d}t\right]\mathrm{d}t, & t \in \left[0, t_{\mathrm{avo}}^3\right), \\[4mm]
y_f(t) = y(0) + \left[a_i - \left(\dfrac{d}{2}\right)\right]\sin\theta(t) + \displaystyle\int_0^t v(t).\sin\left[\theta(0) + \int \Delta\theta(t)\mathrm{d}t\right]\mathrm{d}t & t \in \left[0, t_{\mathrm{avo}}^3\right).
\end{cases}
\tag{26}
$$

3.3.4. Forces Associated with the Boundary Avoidance Process. The boundary avoidance force action process includes boundary avoidance force and boundary avoidance correction force. The trajectory of the boundary avoidance force process is shown in Figure 12. The psychological forces expressed by the dotted line in the states M2, M4, and M6 in Figure 12 indicate the disappearance of the psychological forces at the state.

(1) Boundary Avoidance Force. The boundary avoidance force $F_{b,a}(t)$ is related to the extent to which the front wheel of the vehicle intrudes into the boundary avoidance force influence range. This paper argues that the more severe the extent of front wheel intrusion, the more intense the psychological oppression of the boundary on the rider, the less comfortable and safe the rider feels. The boundary avoidance force is perpendicular to the major semiaxis of the body scope, which does not change the velocity value of the vehicle in the major semiaxis direction, only changes the velocity direction, so that the vehicle moves away from the boundary as soon as possible and enhances the driving comfort.

When the front wheel of the vehicle contact s which is the edge of the avoidance force influence range, other lateral forces disappear and the boundary avoidance force begins to act on the rider. The psychological force expressed by the dotted line of the M2 state in Figure 12 indicates the disappearance of the obstacle avoidance correction force. This paper considers that the value of the boundary avoidance force depends on the distance between the vehicle and the edge of the boundary avoidance force influence range. If the vehicle rides away from the boundary avoidance force influence area, the boundary avoidance force disappears. The psychological force expressed by the dotted line of the M4 state in Figure 11 indicates the disappearance of the boundary avoidance force.

When the front wheel of the vehicle invades the boundary avoidance force influence range, the desired speed of the vehicle will drop significantly. This paper defines the speed change of the vehicle in the boundary avoidance force influence range meets the cosine function change law, where the independent variable $x \in [0, \pi/2]$. The value of vehicle acceleration variation shows a tendency of deceleration followed by acceleration.

The velocity change function within the boundary avoidance force influence range is shown in equation (27). The calculation function of driving force of the vehicle within the boundary avoidance force influence range is shown in equation (28). The calculation function of boundary avoidance force is shown in equation (29). The calculation function of the change rate of body deflection angle under the action of boundary avoidance force is shown in equation (30).

$$
v(t) = \begin{cases}
v\left(t_{\mathrm{bou}}^1\right).\cos\left[0.5\pi\left|\dfrac{\left[y_f(t) - y_b\left(t_{\mathrm{bou}}^1\right)\right]}{y_b\left(t_{\mathrm{bou}}^1\right)}\right|\right], & t \in \left[t_{\mathrm{bou}}^1, t_{\mathrm{bou}}^{\mathrm{tur}}\right), \\[5mm]
v\left(t_{\mathrm{bou}}^{\mathrm{tur}}\right), & t \in \left(t_{\mathrm{bou}}^{\mathrm{tur}}, t_{\mathrm{bou}}^2\right],
\end{cases}
\tag{27}
$$

$$
\overrightarrow{F}_{l,d}(t) = m_i.\dot{v}(t)\overrightarrow{n}_a, \left|y_f(t)\right| \in \left[y_b\left(t_{\mathrm{bou}}^1\right), C_\alpha + \left(\dfrac{w}{2}\right)\right), \alpha \in (l, r)
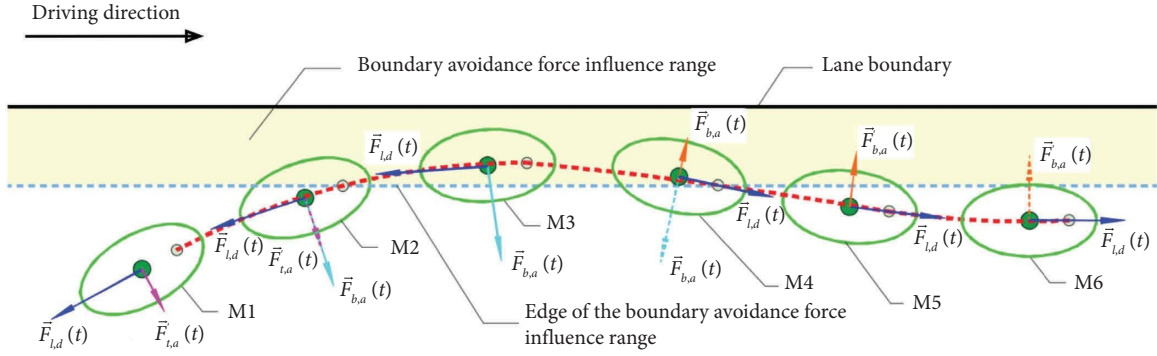\tag{28}
$$

FIGURE 12: Boundary avoidance process trajectory.

$$\overrightarrow{F}_{b,a}(t) = \begin{cases} \psi_i \cdot \exp\left\{ \left| \dfrac{\left[y_f(t) - y_b\left(t_{\text{bou}}^1\right) \right]}{y_b\left(t_{\text{bou}}^1\right)} \right| \right\} \cdot \overrightarrow{n}_v', & \left| y_f(t) \right| \in \left[y_b\left(t_{\text{bou}}^1\right), C_\alpha + \left(\dfrac{w}{2}\right) \right), \alpha \in (l,r), \\[4mm] 0, & \left| y_f(t) \right| \notin \left[y_b\left(t_{\text{bou}}^1\right), C_\alpha + \left(\dfrac{w}{2}\right) \right), \alpha \in (l,r) \end{cases} \tag{29}$$

$$\Delta\theta(t) = \frac{\left\| \overrightarrow{F}_{b,a}(t) \right\|}{\left[m_i \cdot v(t) \right]}, \left| y_f(t) \right| \in \left[y_b(t), C_\alpha + \left(\dfrac{w}{2}\right) \right), \alpha \in (l,r), \tag{30}$$

where ψ_i is the strength of the boundary avoidance force for individual i. The value of ψ_i is a certain value for the specific subject vehicle. t_{bou}^1 is the entry moment when the front wheel of the vehicle crushes the edge of the boundary avoidance force influence range. t_{bou}^2 is the departure moment when the front wheel of the vehicle crushes the edge of the boundary avoidance force influence range. $t_{\text{bou}}^{\text{tur}}$ is the moment when the coordinates of the contact point between the front wheel of the vehicle and the ground reach position $\max(|y_f(t)|)$, $(|y_f(t)| \geq |y_b(t_{\text{bou}}^1)|)$.

(2) Boundary Avoidance Correction Force. The boundary avoidance correction force $F_{b,a}'(t)$ is the accessory force to the boundary avoidance force. The boundary avoidance correction force corrects the vehicle body deflection angle generated by the boundary avoidance force, so that the vehicle body returns to the flow operation direction. The boundary avoidance correction force is perpendicular to the major semiaxis of the body scope, which does not change the vehicle major semiaxis direction velocity value, only changes

the velocity direction, so that the vehicle body deflection angle is corrected to 0 rad and then completes the boundary avoidance process.

The value of the boundary avoidance correction force depends on the distance between the vehicle and the edge of the boundary avoidance force influence range. In general, under the same conditions, the greater the distance, the greater the boundary avoidance correction force. If the vehicle body deflection angle is corrected to 0 rad, the boundary avoidance correction force disappears. As shown in Figure 9, the psychological force expressed by the dotted line of M6 state indicates the disappearance of the boundary avoidance correction force. The calculation function of the boundary avoidance correction force is shown in equation (31). The calculation function of the change rate of vehicle body deflection angle under the influence of boundary avoidance correction force is shown in equation (32). The constraint function of the end moment of the boundary avoidance correction force is shown in equation (33).

$$\theta\left(t_{\text{bou}}^3\right) = \theta\left(t_{\text{bou}}^2\right) + \int_{t_{\text{bou}}^2}^{t_{\text{bou}}^3} \Delta\theta(t)\mathrm{d}t = 0, t_{\text{bou}}^3 > t_{\text{bou}}^2 \geq t_{\text{avo}}^{\text{act}}, \tag{31}$$

$$\overrightarrow{F}_{b,a}'(t) = \begin{cases} \varphi_i \cdot \exp\left\{ \dfrac{\left| y_f(t) - y_b\left(t_{\text{bou}}^1\right) \right|}{\left[W_l - H_{\min}\left(t_{bou}^1\right) - H_{\min}(t) \right]} \right\} \cdot \overrightarrow{n}_v, & t \in \left[t_{\text{bou}}^2, t_{\text{bou}}^3 \right), \\[4mm] 0, & t \in \left[t_{\text{bou}}^3, +\infty \right), \end{cases} \tag{32}$$

$$\Delta\theta(t) = \frac{\left\|\overrightarrow{F}_{b,a}{}'(t)\right\|}{[m_i.v(t)]}, t \in \left[t_{\text{bou}}^2, t_{\text{bou}}^3\right), \tag{33}$$

where φ_i is the strength of the boundary avoidance correction force for individual i. The value of φ_i is a certain value for the specific subject vehicle. t_{bou}^3 is the end moment of boundary avoidance correction force. $t_{\text{avo}}^{\text{act}}$ is the moment

when other lateral forces actually end their action. The function of the vehicle front wheel trajectory after being subjected to the boundary avoidance force is shown in equation (34).

$$\begin{cases} x_f(t) = x\left(t_{\text{bou}}^1\right) - \left[a_i - \left(\dfrac{d}{2}\right)\right]\cos\theta(t) - \displaystyle\int_{t_{\text{bou}}^1}^{t_{\text{bou}}^3} v(t).\cos\left[\int \Delta\theta(t)\mathrm{d}t\right]\mathrm{d}t, \quad t \in \left[t_{\text{bou}}^1, t_{\text{bou}}^3\right), \\[4mm] y_f(t) = y\left(t_{\text{bou}}^1\right) + \left[a_i - \left(\dfrac{d}{2}\right)\right]\sin\theta(t) + \displaystyle\int_{t_{\text{bou}}^1}^{t_{\text{bou}}^3} v(t).\sin\left[\int \Delta\theta(t)\mathrm{d}t\right]\mathrm{d}t, \quad t \in \left[t_{\text{bou}}^1, t_{\text{bou}}^3\right). \end{cases} \tag{34}$$

3.4. Model Logic.
The avoidance process in the model includes four steps, which are discovering nonrigid obstacles and willing to avoid, trajectory judgement, avoidance execution, and trajectory correction. The flowchart is shown in Figure 13.

4. Model Verification

4.1. Data Survey.
Researchers can collect traffic flow parameters and trajectory data of pedestrians, two-wheeled vehicles, and motor vehicles through video filming methods, and among them, using high-definition drone photography methods to conduct traffic flow characteristic surveys is currently the mainstream method. The video data captured by high-definition drones can effectively extract trajectory data and traffic flow characteristic parameters. Moreover, the survey data obtained using drone shooting methods have high quality [37–40]. To investigate the distribution of vehicle speed and related trajectory in the upstream and the road section of flexible obstacle, this paper selects 10 locations of flexible obstacle areas with manhole cover subsidence in Guilin city. Aerial photography investigation is conducted by using an unmanned drone. The relevant indexes of the survey locations are shown in Table 2. Parts of the survey section of the actual views are shown in Figure 14.

In the presurvey, the distribution of the sample of 1103 vehicles leaving the upstream virtual traffic zone was calculated. The upstream virtual traffic zone from which the vehicles leave is concentrated in the interval of 0–14 m (as shown in Figure 15). The marking length of the upstream virtual traffic zone in the survey area is determined to be 16 m.

Statistical methods are often used in the study of traffic flow theory and traffic behavior [37, 41, 42]. As shown in Figure 14, marking lines are set in the upstream 12 m, 16 m from the manhole cover subsidence. Marking lines are also set at the upstream and downstream direction of the transverse central axis of the subsidence at an interval of 2 m along the direction perpendicular to the lane driving. The

marking lines are used to detect the average speeds of the vehicle in the 12–16 m section and through the manhole cover subsidence or the area on both sides. The average speed of the vehicle in the 12–16 m section is defined as the initial speed, and the average speed through the manhole cover subsidence or the area on both sides is defined as the terminal speed.

In this paper, MATLAB software is used to simulate the model, and the simulation step is 0.02 s. Different traffic environments are also constructed, and sensitivity analysis is performed on the model to draw relevant conclusions. The setting parameters of each type of simulated vehicle are shown in Table 3, and the values of the parameters related to the model simulation are shown in Table 4.

In this paper, the process from the beginning of the vehicle avoidance behavior to the front wheel of the vehicle rolling over the edge of the upstream virtual traffic zone or the transverse axis of the flexible obstacle is defined as the avoidance process. The process in which the vehicle is driven by the obstacle avoidance correction force is defined as the correction process.

4.2. Trajectory Simulation

4.2.1. Trajectory Characteristics of Different Strengths of Obstacle Avoidance Force.
In the simulation environment, $C_l = 1.6$ m, riders detect and identify manhole cover subsidence and damage at a distance of 5 m. The vehicles with a deceleration value of more than 1 km/h in the survey data are selected. The average values of initial speed and terminal speed are 6.539 and 5.860, respectively. The acceleration is -0.34 m/s². The speed of the vehicle at the moment the rider detects and identifies the manhole cover subsidence and damage (the speed of the vehicle is $v(0)$, the same below) is deduced as 6.090 m/s, $\theta(0)$ is 0.0349 rad. The simulation vehicle is electric motorcycle. The avoidance behaviors are simulated under the conditions of $\mu_i = 50$ N, 100 N, 150 N, and 200 N, respectively. The simulation trajectory is shown in Figure 16, and the related parameter statistics are shown
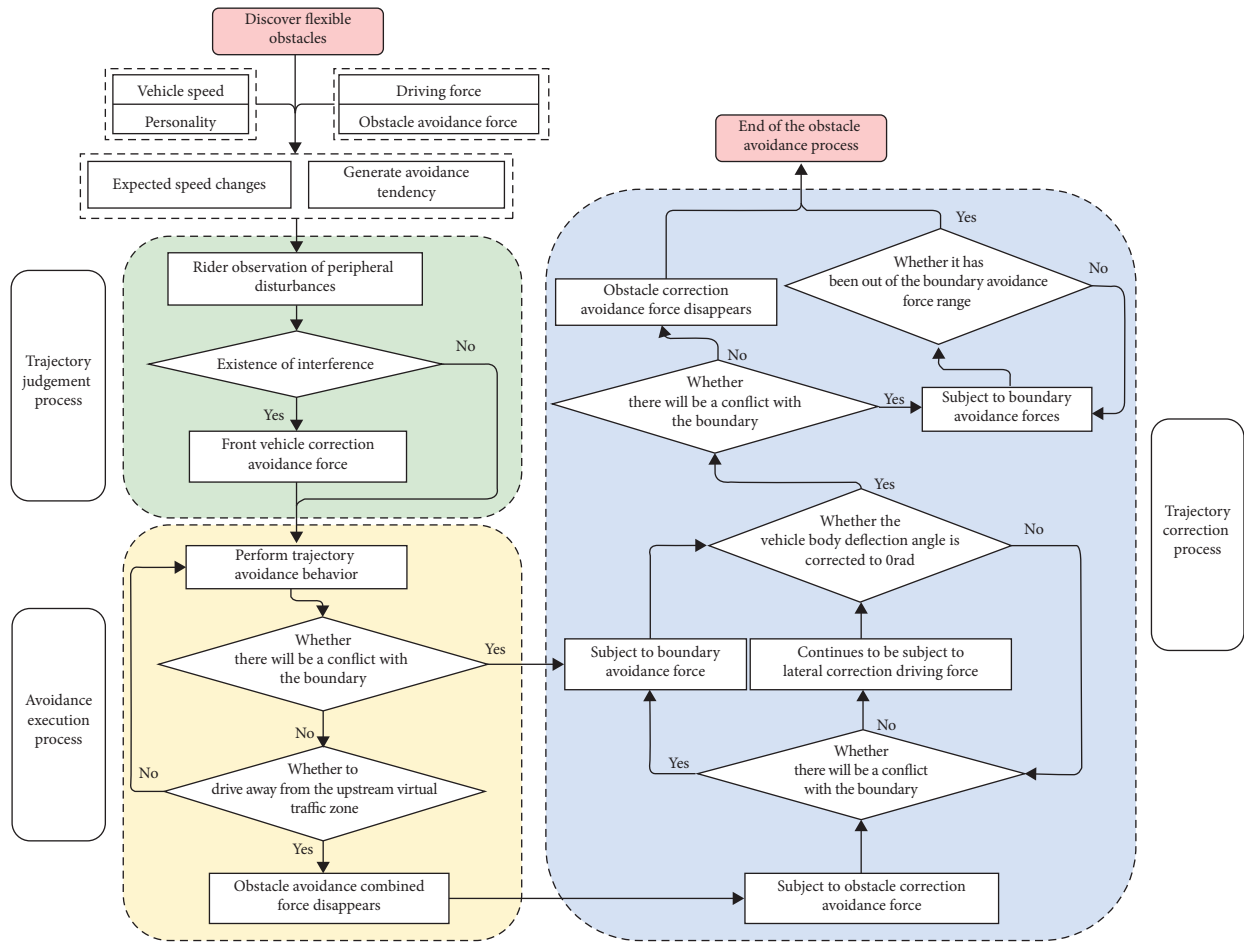
Figure 13: Model logic flow.

Table 2: Partial indicators for survey sites.

No.	Survey section	Isolation facilities	Width of lane (m)	Length of subsidence (m)	Width of subsidence (m)
1	Fangxiang road	Greenbelt	3.0	0.77	0.77
2	Zhongshan middle road	Greenbelt	3.5	0.70	0.70
3	Cuizhu road section A	Greenbelt	3.5	0.72	0.72
4	Jiefang east road section A	Greenbelt	3.5	0.73	0.71
5	Jiefang east road section B	Greenbelt	3.5	0.72	0.73
6	Liuhe road	Greenbelt	4.0	0.72	0.72
7	Cuizhu road section B	Greenbelt	4.5	0.72	0.72
8	Zhongshan north road	Fence	4.5	0.71	0.72
9	Jiefang east road section C	Greenbelt	4.5	0.88	0.86
10	North ring 2st road	Greenbelt	5.0	1.02	0.96

in Figure 17. The statistics related to the avoidance behavior of simulated vehicles under different obstacle avoidance force strength conditions are shown in Table 5. The statistical data in the table include the displacement along the X-axis during the avoidance process of the simulated vehicle, the coordinates of the contact point of the front wheels, and the body deflection angle at the end moment of the avoidance process.

The simulation results show that, under the same conditions, compared with $\mu_i = 50$ N, when $\mu_i = 200$ N, the displacement in the X-axis direction of the simulated vehicle

in the avoidance process is shortened by 26.31%, and the body deflection angle increases by 50.75% at the end moment of the avoidance process.

4.2.2. Avoidance Trajectory Characteristics of Different Vehicle Types. In the simulation environment, $C_l = 1.6$ m, riders detect and identify manhole cover subsidence and damage at a distance of 5 m, the longitudinal coordinate of the center point of the vehicle is 0.1 m. The rider expects to detour to the left of the driving direction. The vehicles with

(1) Actual survey view of Jiefang East Road Section A

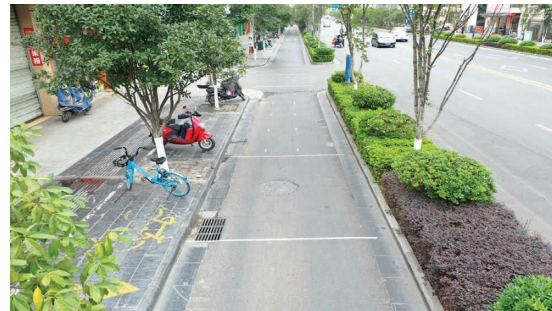(2) Actual survey view of Zhongshan North Road

(3) Actual survey view of Jiefang East Road Section C

(4) Actual survey view of LiuHe Road

(5) Actual survey view of CuiZhu Road

(6) Actual survey view of Zhongshan Middle Road

Figure 14: Part of the survey section of the actual view.

a deceleration value of more than 1 km/h in the survey data are selected. The average values of the initial speed and the terminal speed of each vehicle type are counted in Table 6.

The initial vehicle body deflection angle $\theta(0)$ for all types of vehicles is 0.0349 rad. The strength of the obstacle avoidance force μ_i for all types of vehicles is 150 N. The simulation trajectory is shown in Figure 18, and the related parameter statistics are shown in Figure 19. The statistics related to the avoidance behavior of different vehicle types are shown in Table 7. The statistical data in the table include the displacement along the X-axis during the avoidance process of the simulated vehicle, the coordinates of the contact point of the front wheels, and the body deflection angle at the end moment of the avoidance process.

The simulation results show that, under the same conditions, compared with electric motorcycles, the displacement of the X-axis in the avoidance process of the electric bicycle is shortened by 16.92%, and the body deflection angle

at the end moment of the avoidance process is increased by 13.68%. Compared with electric motorcycles, the displacement of the X-axis in the avoidance process of the human-powered bicycles is shortened by 38.26%, and the body deflection angle at the end moment of the avoidance process is increased by 52.63%.

4.2.3. The Action Process of Boundary Avoidance Force. Three different pavement damages are constructed in different locations in the lane. C_l is 1 m, 0.8 m, 0.6 m, respectively, in three different road scenarios. The simulation vehicle is electric motorcycle. Riders detect and identify manhole cover subsidence and damage at a distance of 4 m. The longitudinal coordinate of the center point of the vehicle is 0 m, the speed of the vehicle is 6 m/s, the expected speed of the vehicle is 5 m/s, the acceleration of the vehicle is -1 m/s^2, $\theta(0)$ is 0.0873 rad, and the strength of the
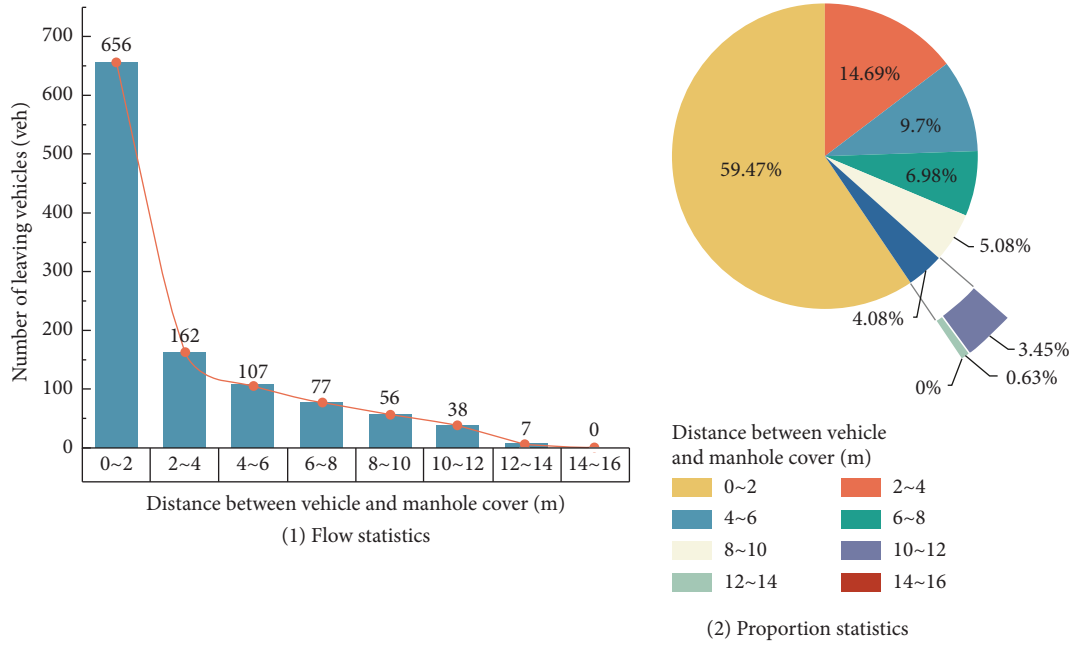
(1) Flow statistics

(2) Proportion statistics

FIGURE 15: Statistics on the number of vehicles leaving each section of the upstream virtual passing zone.

TABLE 3: Simulation parameters for each vehicle type.

Vehicle types	Tire diameter (in)	Tire width (in)	Total vehicle mass (kg)
Electric motorcycle	10	2.125	155 (vehicle 90, rider 65)
Electric bicycle	14	3.0	110 (vehicle 45, rider 65)
Human-powered bicycle	24	1.95	80 (vehicle 15, rider 65)

TABLE 4: Value of the model simulation-related parameters.

Symbols	Names	Values
W_l	Lane width	4.0 m
w	Transverse width of subsidence of manhole cover	0.8 m
C_l	Complete pavement width on the left	0.6 m, 0.8 m, 1.0 m, 1.6 m
μ_i	Strength of obstacle avoidance force	50~200 N
κ_i	Personality correction parameter for the longitudinal length of the frontal influence area	1, 2, 3
t_{rea}	Rider's reaction time	0.7 s [43]
ϕ	Friction coefficient of the tire	0.25 [43]
I_{saf}	Safety distance	0.5 m [43]
ρ_i	Strength of the obstacle avoidance correction force	1.5 μ_i
ψ_i	Strength of the boundary avoidance force	100 N
φ_i	Strength of the boundary avoidance correction force	100 N
$\theta(0)$	Initial vehicle body deflection angle	0 rad, 0.0349 rad, 0.0873 rad

obstacle avoidance force μ_i is 150 N. The simulation trajectory is shown in Figure 20. The simulation trajectory of the boundary avoidance force action process includes three categories: obstacle avoidance trajectory (red trajectory in Figure 20), boundary avoidance trajectory (green trajectory in Figure 20), and boundary correction trajectory (blue trajectory in Figure 20). The related parameter statistics are shown in Figure 21. The statistics related to the avoidance behavior of simulated vehicles under different C_l conditions are shown in Table 8. The statistical data in the table mainly consist of 3 parts: obstacle avoidance data,

boundary avoidance data, and maximum displacement in the Y-axis direction of the front wheel contact point. The obstacle avoidance data and the boundary avoidance data include the displacement in the X-axis direction, the coordinates of the front wheel contact point, and the body deflection angle at the end moment of the avoidance process, respectively.

The simulation results show that, under the same conditions, compared with $C_l = 1.0$ m, when $C_l = 0.6$ m, the displacement in the X-axis direction of the obstacle avoidance is reduced by 78.38%. The body deflection angle at
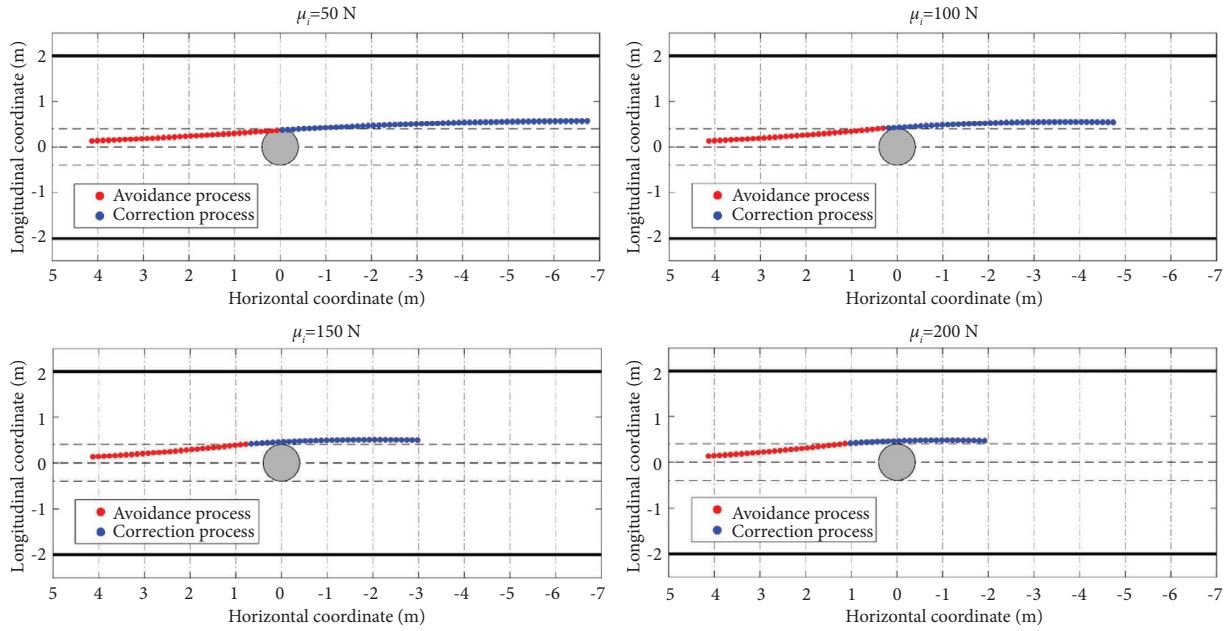
FIGURE 16: Diagram of the front-wheel trajectory of vehicle avoidance behavior under different obstacle avoidance force strength conditions.

the end moment of the avoidance process is decreased by 25.95%. The displacement in the X-axis direction of the boundary avoidance is reduced by 43.42%. The absolute value of the body deflection angle at the end moment of the boundary avoidance is decreased by 57.75%. The maximum displacement in the Y-axis direction of the front wheel contact point of the vehicle is reduced by 75.17%.

4.2.4. The Action Process of Front Vehicle Correction Avoidance Force. The simulation parameters are as follows: the radius of the damage area is 0.4 m, $C_l = 1.6$ m. The subject vehicle B_{obj} in the simulation is electric bicycle. Riders detect and identify manhole cover subsidence and damage at a distance of 10 m. The longitudinal coordinate of the center point of the vehicle is 0.2 m, the speed of the vehicle is 6 m/s, the expected speed of the vehicle is 5 m/s, the acceleration of the vehicle is −0.5 m/s², the initial vehicle body deflection angle $\theta(0)$ is 0 rad, and personality correction parameters κ_i for the longitudinal value of the influencing area in front of the rider are taken as 1, 2, and 3 respectively. The strength of the obstacle avoidance force μ_i is 150 N. The type of the interference vehicle B_{jam} in the simulation is electric bicycle. At the moment $t = 0\,s$, the coordinate of the center point of the vehicle is (7,0.6). The vehicle rides at the uniform speed of 7 m/s. The simulation trajectory at the end moment of the avoidance process is shown in Figure 22, and the statistics of related parameters are shown in Figure 23. The statistics related to the avoidance behavior of different vehicle types are shown in Table 9. The statistics in Table 8 include the displacement along the X-axis during avoidance, the co-ordinates of the front wheel contact point at the end moment of the avoidance, the vehicle body deflection angle, and the distance between B_{obj} and B_{jam} along the X-axis at the end moment avoidance.

The simulation results show that, under the same conditions, compared with $\kappa_i = 1$, when $\kappa_i = 3$, the displacement of B_{obj} along the X-axis in the avoidance increases by 21.39%, and the body deflection angle decreases by 10.84% at the end moment of the avoidance.

4.3. Discussion

(1) As shown in Figures 16 and 17, when the strength of the obstacle avoidance force is greater, representing the stronger the rider's willingness to avoid, the greater the peak value of the vehicle body deflection angle during the avoidance process. The peak value of the vehicle body deflection angle is the maximum vehicle body deflection angle reached by the continuous change during the avoidance process. In the simulation, the rider did not successfully avoid the obstacle at $\mu_i = 50$ N. The smaller the peak value of the vehicle body deflection angle, the smaller the obstacle avoidance correction force and the rider's willingness to correct after the front wheel leaves the upstream virtual traffic zone. The longitudinal displacement and lateral displacement are greater in the correction process. Taubman et al. [44] classified riders into reckless and careless, anxious, angry and hostile, and careful and patient riding styles according to their riding characteristics. According to the relevant definitions in the literature, under the same conditions, the obstacle avoidance force and the obstacle avoidance correction force for reckless and careless riders are smaller. The reckless and careless riders are more tolerant of pavement damage and have a longer time to correct the vehicle body deflection angle after leaving the upstream
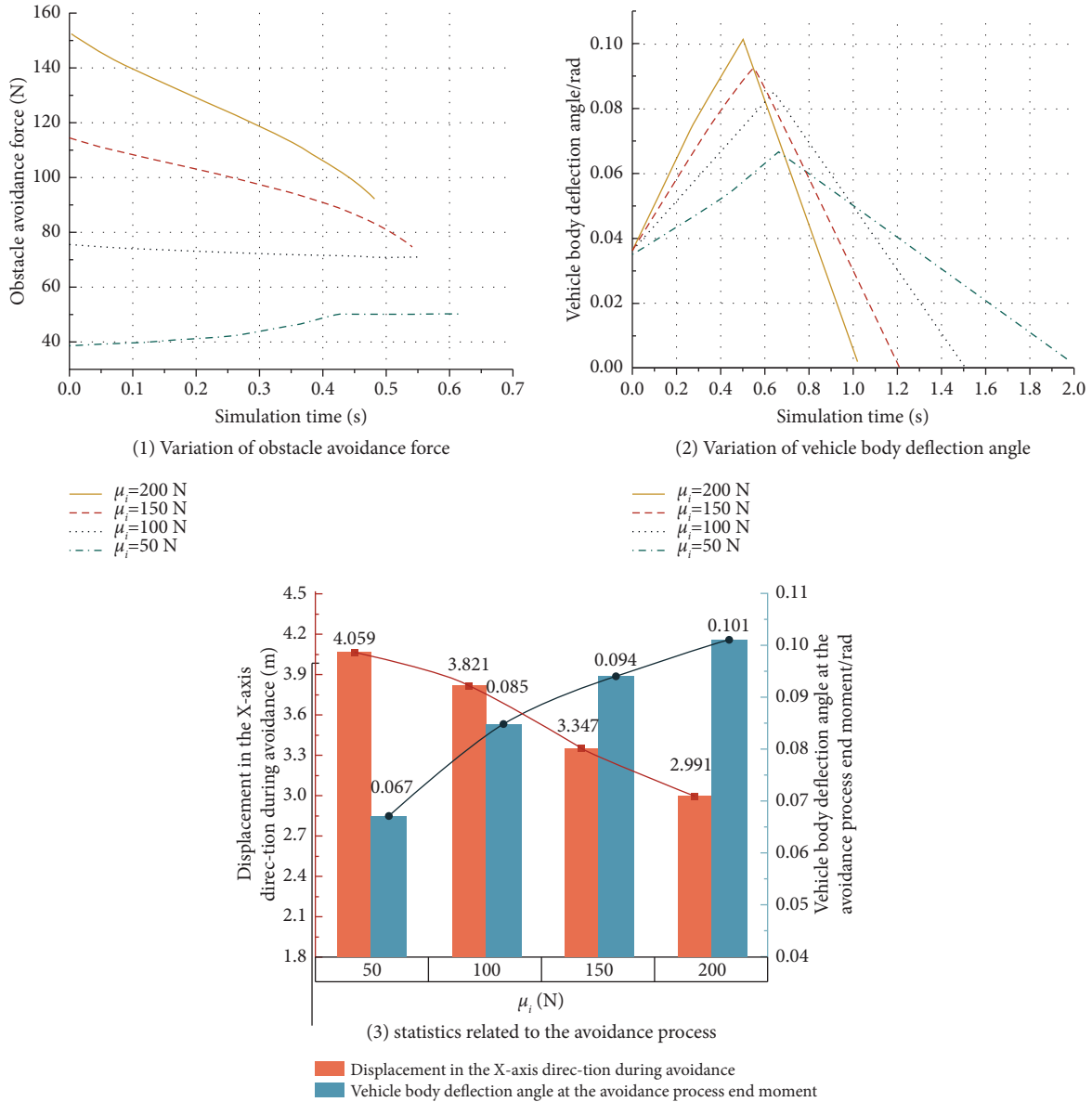
(1) Variation of obstacle avoidance force

μ_i=200 N
μ_i=150 N
μ_i=100 N
μ_i=50 N

(2) Variation of vehicle body deflection angle

μ_i=200 N
μ_i=150 N
μ_i=100 N
μ_i=50 N

(3) statistics related to the avoidance process

■ Displacement in the X-axis direc-tion during avoidance
■ Vehicle body deflection angle at the avoidance process end moment

FIGURE 17: Statistics on parameters related to vehicle avoidance behavior under different obstacle avoidance force strength conditions.

TABLE 5: Statistics on vehicle avoidance behavior under different obstacle avoidance force strength conditions.

μ_i (N)	Displacement in the X-axis direction during avoidance (m)	The coordinate of front wheel contact point at the avoidance process end moment (m)	Vehicle body deflection angle at the avoidance process end moment (rad)	Whether to successfully avoid obstacles
50	4.059	(0.069, 0.363)	0.067	Unsuccessful avoidance
100	3.821	(0.307, 0.407)	0.085	Successful avoidance
150	3.347	(0.780, 0.406)	0.094	Successful avoidance
200	2.991	(1.136, 0.404)	0.101	Successful avoidance

virtual traffic zone. With greater displacement in the Y-axis direction, these types of riders have greater impact on other riders. The obstacle avoidance force and the obstacle avoidance correction force for careful and patient riders are larger. Their tolerance for pavement damage is lower. Careful and patient riders expect to avoid the road damage through the

fastest path and have a shorter time to correct the vehicle body deflection angle after leaving the up-stream virtual traffic zone. The displacement in Y-axis direction is smaller. Careful and patient riders have smaller impact on other riders. The characteristics of the above simulation results are consistent with the actual situation in the survey.

TABLE 6: Speed statistics for each vehicle type.

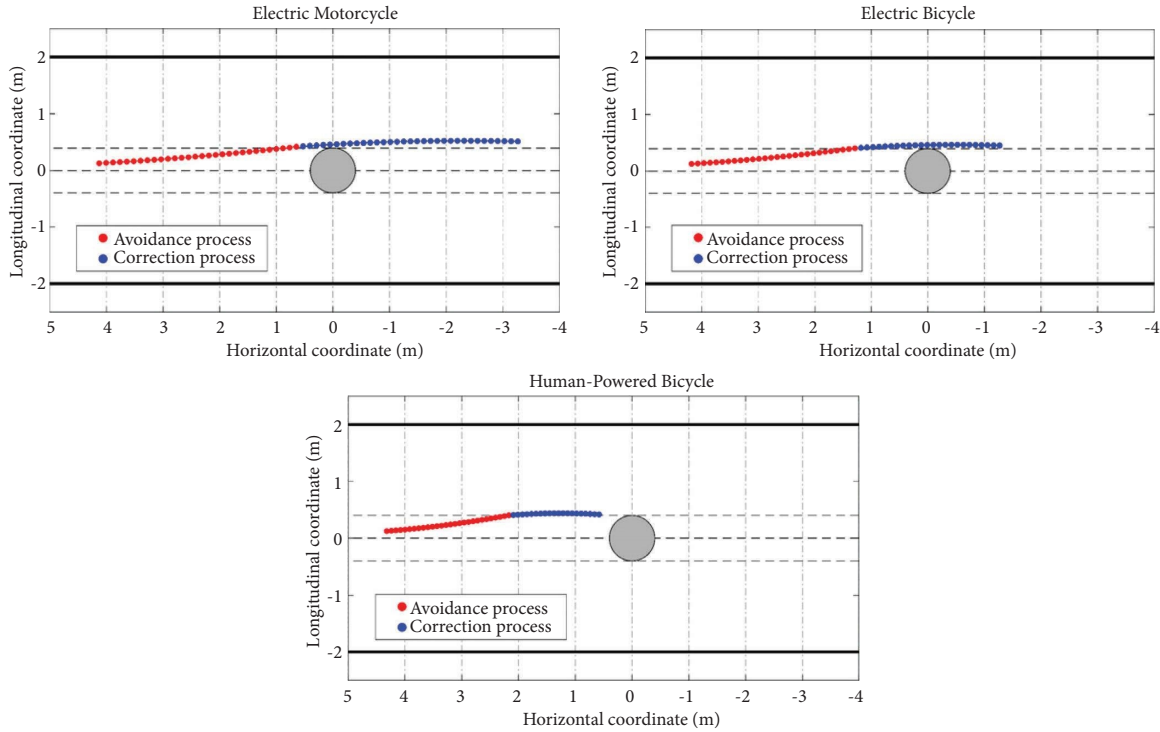| Vehicle type	Initial speed (m/s)	Terminal speed (m/s)	Acceleration (m/s^2)	$v(0)$ (m/s)
Electric motorcycle	6.616	5.924	−0.351	6.122
Electric bicycle	5.813	5.322	−0.230	5.440
Human-powered bicycle	4.323	3.891	−0.129	4.046

FIGURE 18: Diagram of the front-wheel trajectory of vehicle avoidance behavior of different vehicle types.

(2) As shown in Figures 18 and 19, under the same conditions, human-powered bicycles have better avoidance ability and can leave the upstream virtual traffic zone in a shorter distance. Compared to human-powered bicycles, electric motorcycles have poorer avoidance ability and need to leave the upstream virtual traffic zone in a longer distance. During the correction process, the displacement in X-axis direction and Y-axis direction of the electric motorcycle is larger, while the displacement in X-axis direction and Y-axis direction of the human-powered bicycle is smaller. Due to the smaller tire diameter, larger body mass, and faster speed of electric motorcycles, their steering performance is poor. When facing the same pavement damage, electric motorcycles need more distance to avoid obstacle than electric bicycles and human-powered bicycles. The simulation result is consistent with the

actual situation in the survey. The smaller body mass, larger tire diameter, and slower speed of the human-powered bicycle allow it to steer flexibly and complete the avoidance and correction process in a shorter distance. It is found in the survey that human-powered bicycles are the vulnerable group in nonmotorized lanes. The human-powered bicycle riders who successfully avoid obstacles prefer to ride close to the edge of the damaged area to reduce the interference to other vehicles. They also prefer to reduce the change of displacement in the Y-axis direction to preserve their physical strength. The above behavioral characteristics are also reflected in the model.

(3) As shown in Figures 20 and 21, the boundary avoidance force increases as the distance between the vehicle and the lane boundary decreases. The willingness to avoid becomes stronger as the rider
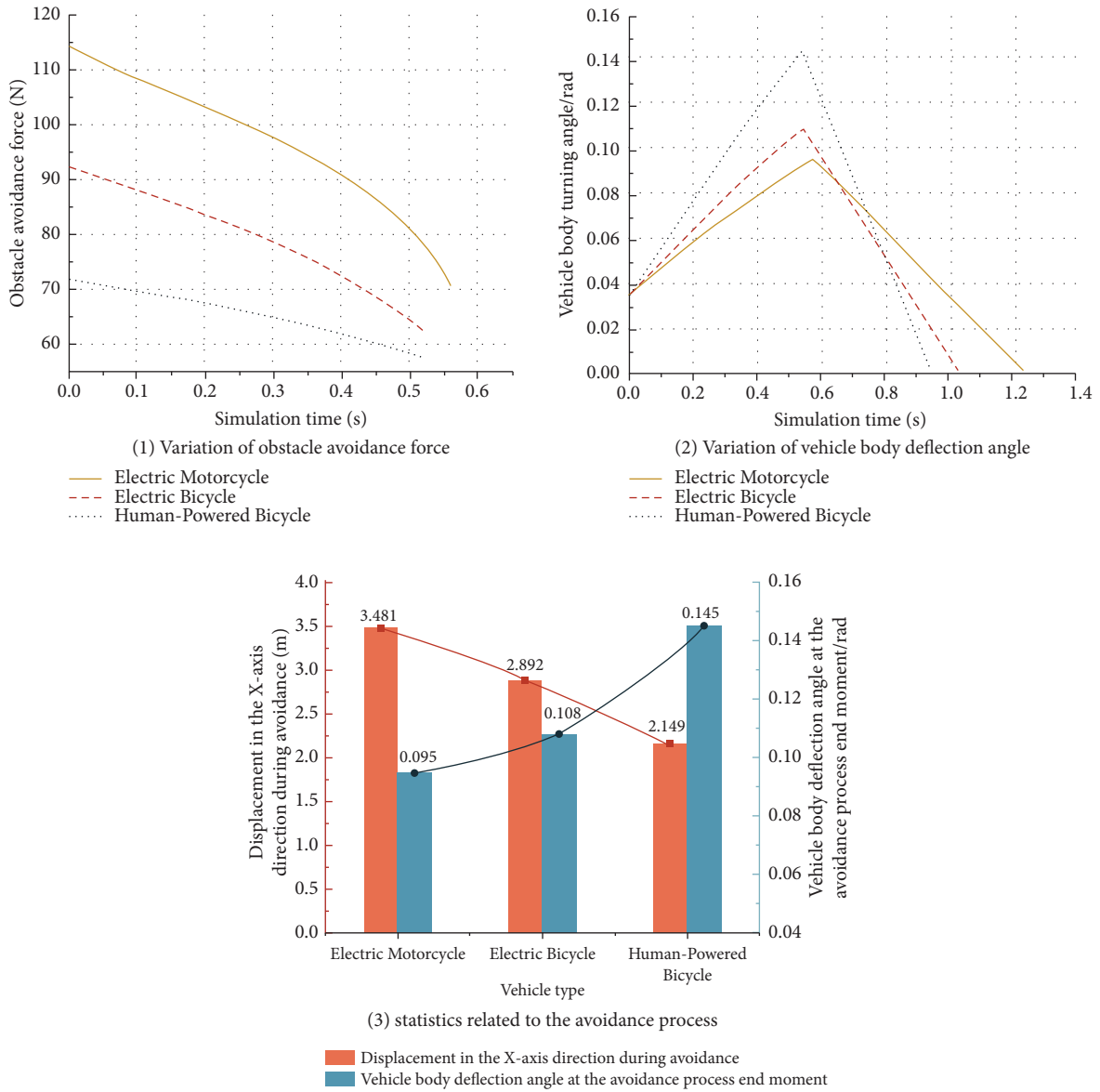
(1) Variation of obstacle avoidance force

— Electric Motorcycle
- - - Electric Bicycle
····· Human-Powered Bicycle

(2) Variation of vehicle body deflection angle

— Electric Motorcycle
- - - Electric Bicycle
····· Human-Powered Bicycle

(3) statistics related to the avoidance process

■ Displacement in the X-axis direction during avoidance
■ Vehicle body deflection angle at the avoidance process end moment

Figure 19: Statistics on parameters related to avoidance behavior of different vehicle types.

Table 7: Statistics related to the avoidance behavior of different vehicle types.

Vehicle type	Displacement in the X-axis direction during avoidance (m)	The coordinate of front wheel contact point at the avoidance process end moment (m)	Vehicle body deflection angle at the avoidance process end moment (rad)
Electric motorcycle	3.481	(0.646, 0.419)	0.095
Electric bicycle	2.892	(1.286, 0.406)	0.108
Human-powered bicycle	2.149	(2.169, 0.401)	0.145
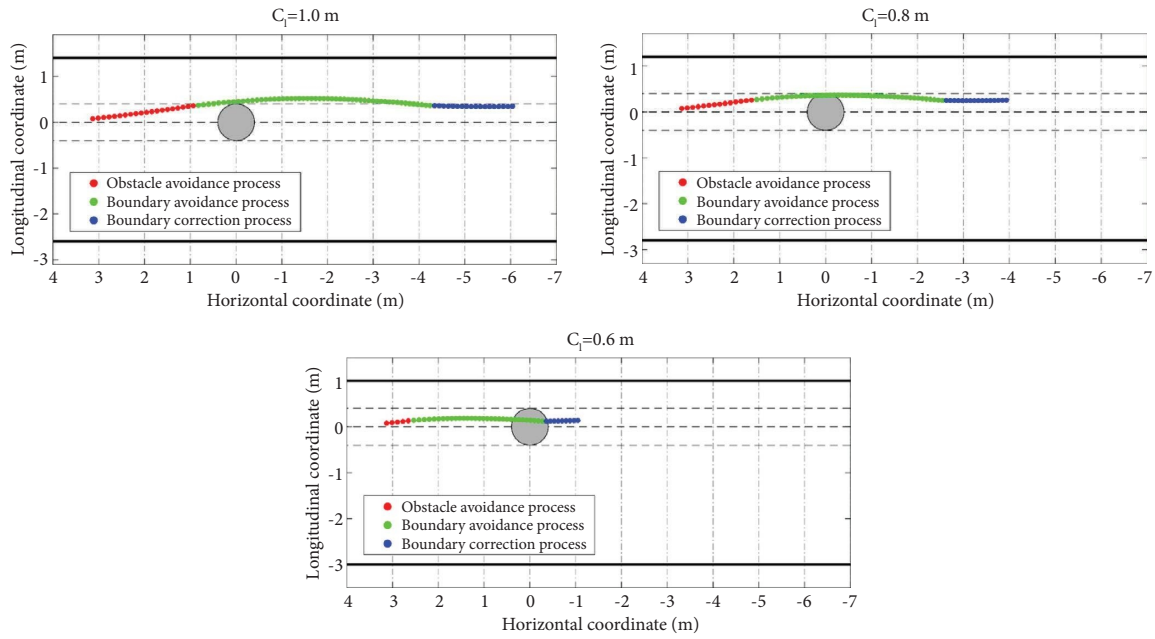
FIGURE 20: Diagram of the front-wheel trajectory of vehicle avoidance behavior under different C_l conditions.
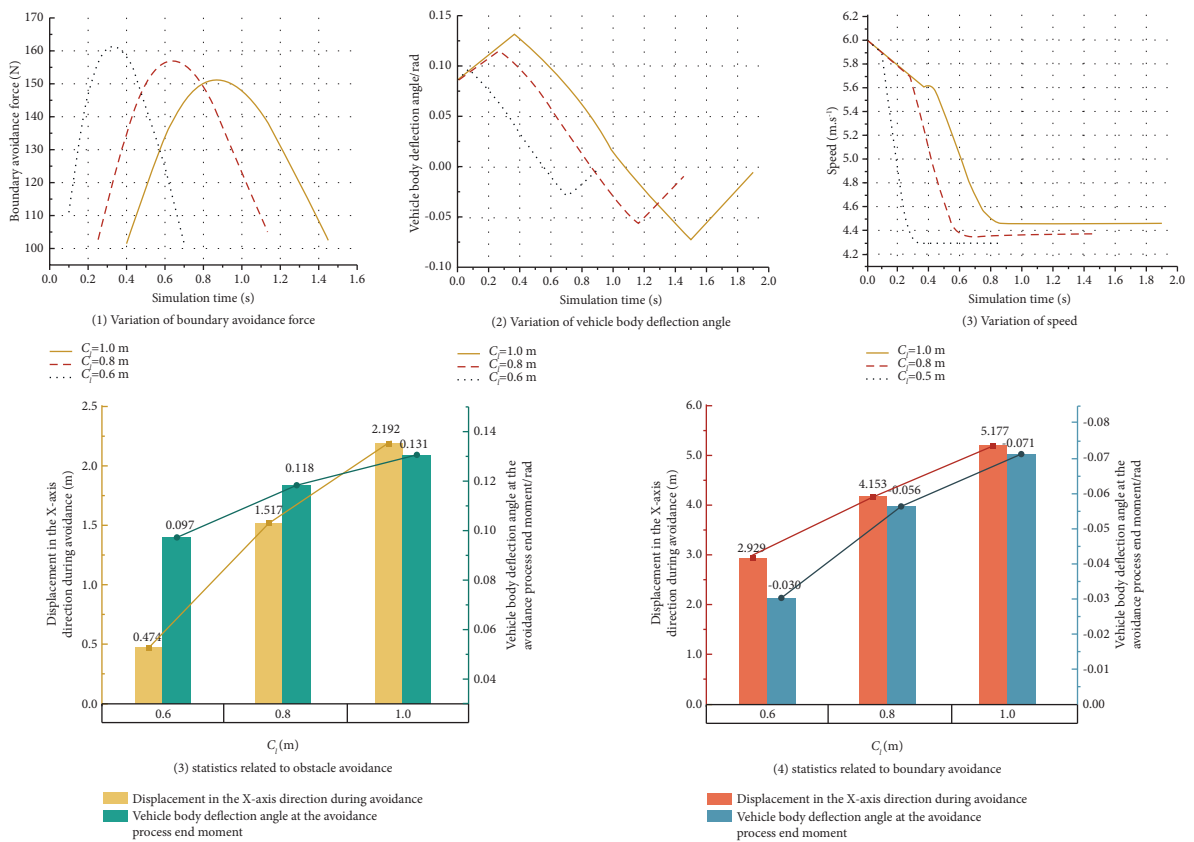

FIGURE 21: Statistics of relevant parameters of vehicle avoidance behavior under different C_l conditions.

Table 8: Statistics of parameters related to vehicle avoidance behavior under different C_l.

| C_l (m)	Obstacle avoidance process			Boundary avoidance process				Whether to successfully avoid obstacles
	Displacement in the X-axis direction during avoidance (m)	The coordinate of front wheel contact point at the avoidance process end moment (m)	Vehicle body deflection angle at the avoidance process end moment (rad)	Displacement in the X-axis direction during avoidance (m)	The coordinate of front wheel contact point at the avoidance process end moment (m)	Vehicle body deflection angle at the avoidance process end moment (rad)	Maximum displacement of front wheel contact point in Y-axis direction (m)	
1.0	2.192	(0.937, 0.358)	0.131	5.177	(−4.240, 0.364)	−0.071	0.439	Successful avoidance
0.8	1.517	(1.612, 0.262)	0.118	4.153	(−2.540, 0.254)	−0.056	0.291	Unsuccessful avoidance
0.6	0.474	(2.656, 0.129)	0.097	2.929	(−0.273, 0.123)	−0.030	0.109	Unsuccessful avoidance
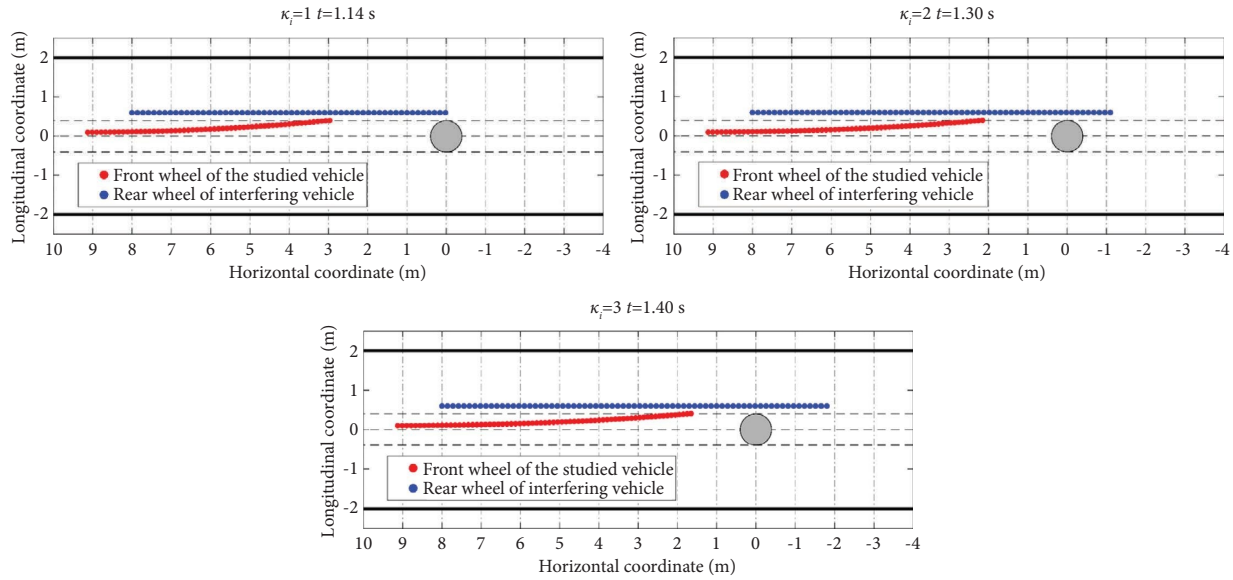
Figure 22: Diagram of the simulation trajectory of vehicle at the end of the avoidance process under different κ_i conditions.

gets closer to the boundary. The vehicle speed decreases rapidly as it approaches the lane boundary, while the vehicle maintains a constant speed as it moves away from the boundary. When the distance is less than 0.8, the rider cannot successfully perform avoidance behavior from the preferred avoidance direction. When the distance is less than 0.6 m, the rider hardly has the will to avoid in the direction and take a straight line to pass through the pavement damage area. Under the same conditions, the closer the edge of the pavement damage in the riders' preferred avoidance direction is to the lane boundary, the greater the boundary avoidance force on the riders and the smaller their willingness to avoid. When the distance reaches a minimal value, the riders no longer

engage in avoidance behavior and pass the pavement damage section. The characteristics of the above simulation results are consistent with the actual situation in the survey.

(4) As shown in Figures 22 and 23, κ_i can reflect the rider's attitude towards riding. The larger the κ_i-value, the more cautious the rider's riding attitude and the more influenced by the interfering vehicles. Careful and patient riders have larger values of κ_i, while reckless and careless riders have smaller values of κ_i. The simulation results show that the larger the value of κ_i, the greater the influence the rider receives from the vehicle in front, and the greater the distance the rider needs to avoid in the X-axis direction. The characteristics of the above simulation results are consistent with the actual situation in the survey.
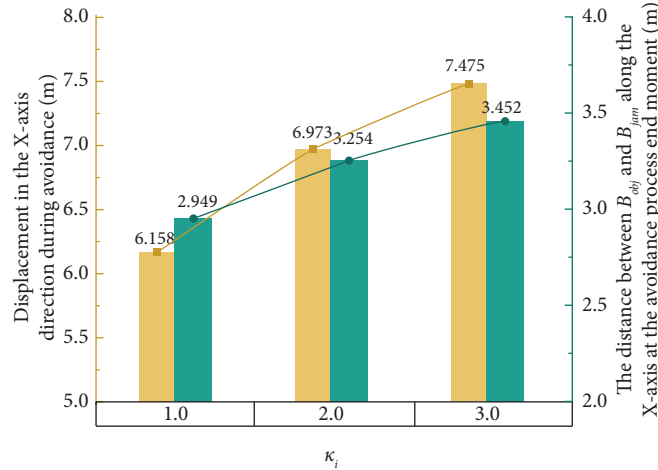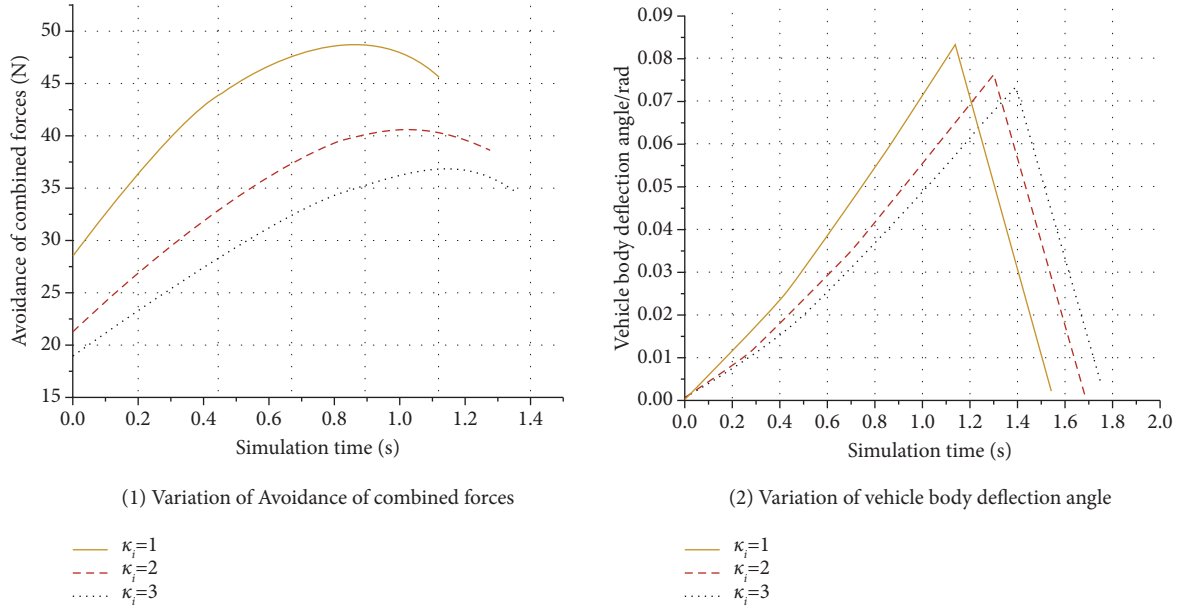
(1) Variation of Avoidance of combined forces

(2) Variation of vehicle body deflection angle

$\kappa_i=1$
$\kappa_i=2$
$\kappa_i=3$

(3) Statistical diagram of data related to obstacle avoidance

Displacement in the X-axis direction during avoidance
The distance between B_{obj} and B_{jam} along the X-axis at the avoidance process end moment

Figure 23: Statistics of parameters related to vehicle avoidance behavior under different κ_i conditions.

Table 9: Statistics of parameters related to vehicle avoidance behavior under different κ_i.

κ_i	Displacement in the X-axis direction during avoidance (m)	The coordinate of front wheel contact point at the avoidance process end moment (m)	Vehicle body deflection angle at the avoidance process end moment (rad)	The distance between B_{obj} and B_{jam} along the X-axis at the avoidance process end moment (m)
1	6.158	(2.969, 0.405)	0.083	2.949
2	6.973	(2.154, 0.403)	0.077	3.254
3	7.475	(1.652, 0.407)	0.074	3.452

5. Conclusion

This paper takes the obstacle avoidance trajectory of two-wheeled vehicle riding in the upstream virtual traffic zone as the research object. The acceleration and deceleration behavior of two-wheeled vehicles and the behavior of steering the vehicle are both abstracted as social force forms. A flexible obstacle avoidance model is established based on the conventional nonmotorized social force model. Different traffic environments are constructed in the model. The model is simulated according to the operation logic, and sensitivity analysis is performed. The simulation vehicle trajectory is plotted. The simulation result characteristics are analyzed. Comparison with the actual situation verifies that the obstacle avoidance model is applicable to describe the essential characteristics of obstacle avoidance in real traffic.

This study only models the trajectory changes of two-wheeled vehicles caused by a single flexible obstacle. Subsequent research will be carried out to address the situation where multiple nonrigid obstacles are distributed in combination on the actual road, as well as to consider the influence of multiple types of obstacles on the overall two-wheeled vehicle trajectory change, which will be carried out in depth step by step. However, the simulation method of obtaining reliable characteristic parameters of two-wheeled vehicle driving trajectory changes by using fine modeling of the social force model can be used as a scientific method for safe driving warning of nonmotorized vehicles and plays a certain role in the development of safety assessment.

Data Availability

The data used to support the findings of this study are available from the corresponding author upon request.

Conflicts of Interest

The authors declare that they have no conflicts of interest.

Acknowledgments

References

[1] D. Helbing and P. Molnár, "Social force model for pedestrian dynamics," *Physical Review A*, vol. 51, no. 5, pp. 4282–4286, 1995.

[2] D. Helbing, A. Johansson, and H. Z. Al-Abideen, "Dynamics of crowd disasters: an empirical study," *Physical Review A*, vol. 75, no. 4, Article ID 46109, 2007.

[3] D. Helbing and P. Mukerji, "Crowd disasters as systemic failures: analysis of the Love Parade disaster," *EPJ Data Sci*, vol. 1, no. 1, p. 7, 2012.

[4] M. Moussaid, D. Helbing, and G. Theraulaz, "How simple rules determine pedestrian behavior and crowd disasters," *Proceedings of the National Academy of Sciences of the U S A*, vol. 108, no. 17, pp. 6884–6888, 2011.

[5] F. Zhang, Z. Song, S. Wu, and J. Qiao, "Pedestrian model combined with detour behavior in multi-obstacles environment," *Systems Engineering-Theory & Practice*, vol. 38, no. 6, pp. 1599–1608, 2018.

[6] J. Li, "Improved social force crowd evacuation simulation model combined with shortest path," *Computer Engineering and Applications*, vol. 57, no. 8, pp. 264–270, 2021.

[7] T. Zhang, D. Bao, T. Zhu, D. Yang, and Z. Di, "Airport passenger queuing model based on social force model," *Systems Engineering and Electronics*, vol. 42, no. 8, pp. 1776–1783, 2020.

[8] S. Zhong, Z. Yu, Y. Yang, C. Sun, and Q. Huang, "Study on evacuation modeling of airport based on social force model," *Journal of System Simulation*, vol. 30, no. 10, pp. 3648–3656, 2018.

[9] X. Wang, R. Zhang, S. Fei, and M. Yang, "Simulation of pedestrian in multifunctional passageway of metro station area based on social foree model," *Journal of System Simulation*, vol. 33, no. 11, pp. 2552–2560, 2021.

[10] L. Hong, J. Gao, S. Qiu, and W. Zhu, "Dynamic simulation on emergency evacuation in metro stations based on improved potential energy field model," *Journal of Tongji University*, vol. 48, no. 3, pp. 398–406, 2020.

[11] J. Wan, J. Sui, and H. Yu, "Research on evacuation in the subway station in China based on the combined social force model," *Physica, A Statistical mechanics and its applications*, vol. 394, no. 2, pp. 33–46, 2014.

[12] M. Zou, T. Zhou, and D. Wang, "Rest facility layout of evacuation roads based on the social force model in chongqing commercial center," *Safety and Environmental Engineering*, vol. 28, no. 6, pp. 91–99+108, 2021.

[13] N. Cao, L. Zhao, Z. Qu, Y. Chen, Q. Bai, and X. Deng, "Social force model considering bi-direction pedestrian slipstreaming behavior," *Journal of Jilin University (Engineering and Technology Edition)*, vol. 49, no. 3, pp. 688–694, 2019.

[14] Y. Zhou, Z. Zhou, Y. Xu, and Y. Cai, "A model for crossing behaviors of pedestrians at intersections during flashing green signals," *Journal of Transport Information and Safety*, vol. 36, no. 1, pp. 74–80, 2018.

[15] W. Wu, Z. Wang, and F. Ma, "Simulation analysis of evolutionary game of pedestrians' group behaviors under influence of herd behavior: in case of crossing behavior," *Journal of Jilin University (Engineering and Technology Edition)*, vol. 47, no. 1, pp. 92–96, 2017.

[16] X. Liang, B. Mao, and Q. Xu, "Psychological-physical force model for bicycle dynamics," *Journal of Transportation Systems Engineering and Information Technology*, vol. 12, no. 2, pp. 91–97, 2012.

[17] Y. Zheng, *Rider's Heterogeneity-Based Microscopic Modeling and Simulation of Non-motorized Flow in Complex Traffic Environment*, Southeast university, Dhaka, Bangladesh, 2020.

[18] S. Li, *Research on the Microscopic Behavior Models of Vehicle, Bicycle, Pedestrian, and Their Interactive Interferences at the Signalized Plane Intersection*, Beijing Jiaotong University, Beijing, China, 2013.

[19] M. Li, F. Shi, and D. Chen, "Analyze bicycle-car mixed flow by social force model for collision risk evaluation," in *Proceedings*

of the The 3rd International Conference on Road Safety and Simulation, Indianapolis, IN, USA, September 2011.

[20] Z. Qu, N. Cao, Y. Chen, L. Zhao, Q. Bai, and R. Luo, "Modeling electric bike–car mixed flow via social force model," Advances in Mechanical Engineering, vol. 9, no. 9, Article ID 168781401771964, 2017.

[21] R. Schönauer, M. Stubenschrott, W. Huang, C. Rudloff, and M. Fellendorf, "Modeling concepts for mixed traffic: steps toward a microscopic simulation tool for shared space zones," Transportation Research Record, vol. 2316, no. 1, pp. 114–121, 2012.

[22] D. Yang, X. Zhou, C. Wen, M. Lv, and S. Liu, "Modeling and simulation of motor vehicle-electric bicycle traffic flow at signalized intersection," Journal of Harbin Institute of Technology, vol. 50, no. 8, pp. 181–187, 2018.

[23] C. Dias, H. Nishiuchi, S. Hyoudo, and T. Todoroki, "Simulating interactions between pedestrians, Segway riders and cyclists in shared spaces using social force model," Transportation Research Procedia, vol. 34, pp. 91–98, 2018.

[24] Y. Hao, R. Liu, H. Hu, Y. Fang, and Z. Liu, "One-way pedestrian-bicycle mixed flow model and self-organization Phenomenon," Journal of Transportation Systems Engineering and Information Technology, vol. 22, no. 2, pp. 223–229, 2022.

[25] J. Zhu and S. Chen, "An improved social force model considering bicycle conflicts at intersection," Journal of Chongqing Jianzhu University, vol. 38, no. 12, pp. 18–25, 2019.

[26] Z. Wang, L. Zhao, Y. Jiao, and N. Cao, "Social force model of pedestrian-bike mixed flow at signalinalized crosswalk," Journal of Jilin University (Engineering and Technology Edition), vol. 48, no. 1, pp. 87–97, 2018.

[27] R. Zhang, H. Jiatian, S. Zhang, and S. Cheng, "An improved social force model considering the shift and deceleration of the overtaken non-motorized vehicle," Science Technology and Engineering, vol. 22, no. 34, pp. 15367–15371, 2022.

[28] X.-R. Wang, Y.-S. Deng, F. Xu, M. Xiao, and L. Meng, "Simulation and optimization of passenger flow organization in subway station based on improved social force model," Bulletin of Science and Technology, vol. 38, no. 10, pp. 101–107+124, 2022.

[29] M. Shang, R. Zhang, Z. Qi, and H. Jiatian, "Research on improvement of social force modelof opposite pedestrian avoidance and contact behavior," Computer Simulation, vol. 38, no. 3, pp. 63–67+77, 2022.

[30] Z. Kang, L. Zhang, and K. Li, "An improved social force model for pedestrian dynamics in shipwrecks," Applied Mathematics and Computation, vol. 348, pp. 355–362, 2019.

[31] W. Zeng, P. Chen, H. Nakamura, M. Iryo-Asano, and Miho, "Application of social force model to pedestrian behavior analysis at signalized crosswalk," Transportation Research Part C: Emerging Technologies, vol. 40, pp. 143–159, 2014.

[32] D. R. Parisi, M. Gilman, and H. Moldovan, "A modification of the Social Force Model can reproduce experimental data of pedestrian flows in normal conditions," Physica A: Statistical Mechanics and Its Applications, vol. 388, no. 17, pp. 3600–3608, 2009.

[33] L. Huang, Z. Wu, H. Pei-xin, R. Zhang, and J. Wu, "Research on UAV traffic state perception method based on air-ground information fusion," China Journal of Highway and Transport, vol. 34, no. 12, pp. 249–261, 2021.

[34] V. Cossalter, Motorcycle Dynamics, Lightning Source Inc, LaVergne, TN, USA, Second edition, 2006.

[35] F. P. D. Navin, "Bicycle traffic flow characteristics: experimental results and comparisons," ITE Journal-Institute of Transportation Engineers, vol. 64, no. 3, pp. 31–37, 1994.

[36] X. Yan, Study on Operational Characteritstics of Mixed Bicycle Traffic Flow and Design Optimization of Bicycle Lane, Southeast university, Dhaka, Bangladesh, 2017.

[37] S. Wu, Y. Zou, L. Wu, and Y. Zhang, "Application of Bayesian model averaging for modeling time headway distribution," Physica A: Statistical Mechanics and Its Applications, vol. 620, Article ID 128747, 2023.

[38] I. Sheng, D. Wang, Y.-H. Chen, and D. Sun, "Pedestrian movement trajectory reappearance and crossing feature expression based on video processing," Journal of Southeast University, vol. 42, no. 6, pp. 1233–1237, 2012.

[39] L. Huang, Z. Huang, W. Ze-rong et al., "Comparison of data-driven human-like driving models under different behavior model frameworks," Journal of South China University of Technology, vol. 50, no. 10, pp. 1–10, 2022.

[40] Y. Lu, Y. Zou, K. Cheng, L. Zheng, S. Selpi, and T. Zhu, "Analytical method of traffic conflict at urban road intersections based on risk region," Journal of Tongji University, vol. 49, no. 7, pp. 941–948, 2021.

[41] X. Ye, Y. Chang, T. Wang, X. Yan, L. Song, and J. Chen, "Research on parking app choice behavior based on MNL," Travel Behaviour and Society, vol. 25, pp. 174–182, 2021.

[42] X. Ye, X. Sui, T. Wang, X. Yan, and J. Chen, "Research on parking choice behavior of shared autonomous vehicle services by measuring users' intention of usage," Transportation Research Part F: Traffic Psychology and Behaviour, vol. 88, pp. 81–98, 2022.

[43] China Higway and Transportation Society, Transportation Engineering Handbook, China Communications Press, Beijing, China, 1998.

[44] O. Taubman- Ben-Ari and V. Skvirsky, "The multidimensional driving style inventory a decade later: review of the literature and re-evaluation of the scale," Accident Analysis & Prevention, vol. 93, pp. 179–188, 2016.